ECCOMAS Congress 2016
VII European Congress on Computational Methods in Applied Sciences and Engineering
M. Papadrakakis, V. Papadopoulos, G. Stefanou, V. Plevris (eds.)
Crete Island, Greece, 5–10 June 2016

A NEW SHELL FINITE ELEMENT WITH DRILLING DEGREES OF FREEDOM AND ITS RELATION TO EXISTING FORMULATIONS

Robert Winkler[1], **Dimitrios Plakomytis**[1,2]

[1]Institute of Mechatronics, University of Innsbruck
Technikerstrasse 13, 6020 Innsbruck
e-mail: Robert.Winkler@uibk.ac.at

[2] INTALES GmbH
Innsbrucker Strasse 1, 6161 Natters
e-mail: Dimitrios.Plakomytis@uibk.ac.at

Keywords: Shell theory, drill rotation, rotation constraint, Allman shape functions

Abstract. *This contribution deals with shell element formulations involving three rotational degrees of freedom. Its purpose is twofold. Firstly, a review of relevant non-linear shell theories as well as finite element implementations is given and corresponding defects are addressed. Secondly, a geometrically linear shell element formulation is presented which is free of any of these defects. Conventional shell theories involve two rotational degrees of freedom, the drilling rotation being excluded. Three standard methods of incorporating the drilling degree of freedom are considered: (a) The application of a proper rotation constraint condition, (b) shell theories intrinsically involving three rotational degrees of freedom (here called 'micropolar theories') and (c) introducing the drilling degree of freedom at the level of the finite element discretization (Allman-type shape functions). Here, reference implementations relying on approaches (a) to (c) as well as their reasonable combinations are considered. It is demonstrated that each of these implementations reveals at least one questionable feature: Formulations based on a micropolar approach involve ad hoc assumptions related to the constitutive law. Formulations involving a rotation constraint imply the application of a problem-dependent penalty or regularization parameter. Finally, Allman-type shell elements suffer from a lower convergence rate for bending dominated problems compared to isoparametric ones. The proposed shell element relies on a conventional (nonpolar) shell theory and applies a drill rotation constraint via a penalty formulation. A crucial point is the application of properly designed enhanced strain fields to avoid in-plane locking phenomena. It is demonstrated numerically that the resulting implementation overperforms existing shell elements. Most importantly, the way of incorporating the rotation constraint proves to constitute a proper penalty formulation in the sense that for sufficiently large values of the penalty parameter the results are independent of the latter. Moreover, this threshold is independent of the problem. The relation to existing implementations of the drill rotation constraint, all of them requiring the application of problem dependent penalty parameters, is discussed. Concluding, it is explicated how the present formulation derives from a micropolar approach.*

1 Introduction

From a practical point of view, it is generally agreed that shell finite elements with six degrees of freedom (dofs) at each node exhibit substantial advantages compared to those with just five dofs or even those with a varying number (5/6 dof formulations). From a theoretical or numerical point of view, some aspects of 6 dof formulations still deserve additional clarification. The implementation of the additional dof, i.e. the so called 'drilling' rotation, is achieved either by constraining the drilling dof to the in-plane rigid-body rotation (a), applying shell theories intrinsically involving three rotational degrees of freedom (b), or on the level of the finite element discretization applying so-called Allman-type shape functions (c).

State-of-the-art shell finite element formulations are based on mixed variational principles, the Hu-Washizu principle, e.g. In contrast to formulations relying on the total potential energy, these mixed formulations involve incompatible stress and/or strain fields, leading to hybrid, enhanced strain, or mixed formulations which are largely free of locking effects. The comparison of the different approaches if performed at three levels: At the level of the strong formulation (shell theory), at the level of the weak formulation (variational principle), and at the level of the finite element discretization.

The remainder of the paper herein is organised as follows. Section 2 elaborates on different approaches for deriving shell models but more importantly illustrates the main differences of these approaches. Further, in Section 3 three methods for the incorporation of the drill degree of freedom for two-dimensional shell models are discussed. The relation of the drill RC formulations with 6 dof shell models is outlined. Then a brief discussion on the corresponding finite element approximations is provided in Section 4. Further, in Section 5 two alternative implementations of the drill RC are described. The various implementations are tested through a multitude of benchmark examples and the results are presented in Section 6. Closing, a discussion based on the numerical results is provided in Section 7.

2 Shell Theories

One of the first fruitful attempts to derive a consistent theory of thin shells is due to Koiter [20]. Since then, tremendous efforts have been devoted to this topic. A preliminary conclusion of this development has been given in the monograph of Libai and Simmonds [21]. During the past years the number of new contribution has decreased significantly. Recent trends rather deal with smart shell structures [6], micropolar theories [1], and thermodynamics [13].

One way of deriving various shell mathematical models is through the use of 3D Continuum mechanics. Here the two most commonly applied categories of shell theories are considered: The first one can be traced back to Green and Zerna [15] who gave the first general linear theory of shells applying tensor calculus. Its non-linear counterpart has been derived by Simo et al. [32], [33] , [34]. The theory employs symmetric membrane and bending strain measures derived from the Green-Lagrange strain tensor. Recently, this theory has been revisited by Wagner and Gruttmann [36] to obtain a high-end finite element implementation. Commonly this approach is attributed as *geometrically exact shell theory*. An alternative point of departure has been provided by Reissner [26]. It has been recast by Ibrahimbegovic [17]. Via the application of a non-symmetric Biot-type strain measures the drilling dof enters the virtual work principle. Here these type of shell theories are called *micropolar*. It is emphasized that the micro-rotations enter at the level of dimensionaly reduced shell theory rather than at the level of 3D continuum mechanics.

A third type of shell theories is due to Simmonds [28] and has been elaborated by Chroscieliewsky et. al. [9]. Unlike in the other approaches, no kinematic assumptions (such as the Reissner-Mindlin assumption) are considered. It leads to almost the same expressions as the aforementioned approach, except for the appearance of drill moments, non-symmetric bending moments, and—in principle—to a non-local constitutive relation. Since the shell balance equations are exact consequences of the principle of virtual work, this type of theory is sometimes called *statically exact*. All approximations are transferred to the constitutive relation.

2.1 Description of the Shell Geometry and Kinematics

The position vector of any material point of the undeformed shell body $\mathcal{B}_0$ is written as

$$\mathbf{X}(\theta^i) = \mathbf{\Phi}(\theta^\alpha) + \theta \mathbf{D}(\theta^\alpha), \tag{1}$$

where $|\mathbf{D}(\theta^\alpha)| = 1$ and $h_- \leq \theta \leq h_+$ with $h = h_+ - h_-$ being the shell thickness. Further, $\mathbf{\Phi}(\theta^\alpha)$ denotes the position vector of the shell mid surface and (θ^i) is a curvilinear co-ordinate system parametrizing the shell body. Greek indices $\alpha, \beta, \ldots$ always range from 1 to 2. Latin indices $i, j, \ldots$ range from 1 to 3. Einstein's summation convention is used in the sequel. Introducing a kinematic assumption according to the well-known Reissner-Mindlin plate theory, the position vector of the material point in the deformed configuration $\mathcal{B}_\kappa$ is,

$$\mathbf{x}(\theta^i) = \boldsymbol{\phi}(\theta^\alpha) + \theta \mathbf{d}(\theta^\alpha), \tag{2}$$

where $|\mathbf{d}(\theta^\alpha)| = |\mathbf{D}(\theta^\alpha)| = 1$.

The covariant tangent vectors in the reference configuration read,

$$\mathbf{G}_\alpha = \mathbf{X}_{,\alpha} = \mathbf{\Phi}_{,\alpha} + \theta \mathbf{D}_{,\alpha}, \qquad \mathbf{G}_3 = \mathbf{X}_{,3} = \mathbf{D} \tag{3}$$

where $(\cdot)_{,\alpha} = \partial(\cdot)/\partial\theta^\alpha$ denotes the partial derivative. According to Eq. (2), the basis vectors of the current configuration are

$$\mathbf{g}_\alpha = \mathbf{x}_{,\alpha} = \boldsymbol{\phi}_\alpha + \theta \mathbf{d}_{,\alpha} \qquad \mathbf{g}_3 = \mathbf{x}_{,3} = \mathbf{d} \tag{4}$$

The corresponding basis vectors at the reference surface are denoted by $\mathbf{A}_\alpha = \mathbf{\Phi}_{,\alpha}$ and $\mathbf{a}_\alpha = \boldsymbol{\phi}_{,\alpha}$, respectively. Further, the contravariant basis vectors $\mathbf{G}^i$, $\mathbf{g}^i$, $\mathbf{A}^i$, and $\mathbf{a}^i$ are defined via $\mathbf{G}^i \cdot \mathbf{G}_j = \delta^i_j$, $\mathbf{A}^\alpha \cdot \mathbf{A}_\beta = \delta^\alpha_\beta$, etc. with δ^i_j being the Kronecker delta. The area and volume element in the undeformed configuration are

$$dA_0 = \sqrt{A}\, d\theta^1 d\theta^2, \qquad dV_0 = \sqrt{G}\, d\theta^1 d\theta^2 d\theta, \tag{5}$$

where $\sqrt{A} = \|\mathbf{A}_1 \times \mathbf{A}_2\|$ and $\sqrt{G} = \|\mathbf{G}_1 \times \mathbf{G}_2\|$. The elements dA and dV for the deformed configuration are defined analogously. Spatial and surface base vectors are related via $\mathbf{G}_\alpha = Z^\gamma_\alpha \mathbf{A}_\gamma$, where Z^γ_α are the components of the *shifter tensor* $\mathbf{Z} = Z^\gamma_\alpha \mathbf{Z}_\gamma \otimes \mathbf{A}^\alpha = \mathbf{G}_\alpha \otimes \mathbf{A}^\alpha$. Its determinant $Z = |Z^\gamma_\alpha| = \sqrt{G/A}$ is used to relate dA_0 and dV_0,

$$dV_0 = Z\, d\theta\, dA_0 \tag{6}$$

Analogously relations hold for the deformed configuration.

2.2 Shell Kinematics Based on Symmetric Green-Lagrange Strains

In the context of convective coordinates, the Green-Lagrange strain tensor reads

$$\mathbf{E} = E_{ij}\mathbf{G}^i \otimes \mathbf{G}^j, \quad E_{ij} = \frac{1}{2}(g_{ij} - G_{ij}), \tag{7}$$

Its components with respect to the basis $(\mathbf{G}^i)$ are

$$\begin{aligned} E_{\alpha\beta} &= \frac{1}{2}(\mathbf{g}_\alpha \cdot \mathbf{g}_\beta - \mathbf{G}_\alpha \cdot \mathbf{G}_\beta) = \varepsilon_{\alpha\beta} + \theta\kappa_{\alpha\beta} + \theta^2\rho_{\alpha\beta} \\ E_{\alpha 3} &= \frac{1}{2}(\mathbf{g}_\alpha \cdot \mathbf{g}_3 - \mathbf{G}_\alpha \cdot \mathbf{G}_3) = \gamma_\alpha \\ E_{33} &= \frac{1}{2}(\mathbf{g}_3 \cdot \mathbf{g}_3 - \mathbf{G}_3 \cdot \mathbf{G}_3) = 0 \end{aligned} \tag{8}$$

where

$$\begin{aligned} \varepsilon_{\alpha\beta} &= \frac{1}{2}(\mathbf{a}_\alpha \cdot \mathbf{a}_\beta - \mathbf{A}_\alpha \cdot \mathbf{A}_\beta) \\ \kappa_{\alpha\beta} &= \frac{1}{2}(\mathbf{a}_\alpha \cdot \mathbf{d}_{,\beta} + \mathbf{a}_\beta \cdot \mathbf{d}_{,\alpha} - \mathbf{A}_\alpha \cdot \mathbf{D}_{,\beta} - \mathbf{A}_\beta \cdot \mathbf{D}_{,\alpha}) \\ \gamma_\alpha &= \frac{1}{2}(\mathbf{a}_\alpha \cdot \mathbf{d} - \mathbf{A}_\alpha \cdot \mathbf{D}), \end{aligned} \tag{9}$$

are the membrane, bending, and transverse shear strains, respectively. It turns out that the second order strains $\rho_{\alpha\beta}$ do not enter the virtual work expression. (Note that this in *not* an approximation!) With the variation of the Green-Lagrange strain components

$$\delta E_{ij} = \frac{1}{2}(\delta\mathbf{g}_i \cdot \mathbf{g}_j + \mathbf{g}_i \cdot \delta\mathbf{g}_j) \tag{10}$$

the virtual strain energy for a deformable body reads

$$\delta W_{int} = \int_{\mathcal{B}_0} \mathbf{S} : \delta\mathbf{E}\, dV_0 \tag{11}$$

In terms of convective coordinates, the 2^{nd} Piola-Kirchoff (PK2) stress tensor is given by

$$\mathbf{S} = j\sigma^{ij}\mathbf{G}_i \otimes \mathbf{G}_j \tag{12}$$

where $j = dV/dV_0 = \sqrt{g/G}$ and σ^{ij} are the components of the Cauchy stress tensor. Substituting the kinematic assumption Eq. (4) into Eq. (10) and the latter into Eq. (11) straight-forward calculations yield

$$\delta W_{int} = \int [\mathbf{n}^\alpha \cdot \delta\mathbf{a}_\alpha + \mathbf{m}^\alpha \cdot \delta\mathbf{d}_{,\alpha} + \mathbf{q} \cdot \delta\mathbf{d}] \sqrt{a}\, d\theta^1 d\theta^2 \tag{13}$$

Therein, the stress resultants

$$\mathbf{n}^\alpha = \int_{h_-}^{h_+} \sigma^{j\alpha}\mathbf{g}_j z\, d\theta, \quad \mathbf{m}^\alpha = \int_{h_-}^{h_+} \sigma^{j\alpha}\mathbf{g}_j \theta z\, d\theta, \quad \mathbf{q} = \int_{h_-}^{h_+} \sigma^{j3}\mathbf{g}_j z\, d\theta \tag{14}$$

have been defined. Again, applying Eq. (4), the membrane force vectors, bending moments, and transverse shear forces can be written as

$$\mathbf{n}^\alpha = n^{\beta\alpha}\mathbf{a}_\beta + q^\alpha \mathbf{d}, \qquad \mathbf{m}^\alpha = m^{\gamma\alpha}\mathbf{a}_\gamma + m^{3\alpha}\mathbf{d}, \qquad \mathbf{q} = \tilde{q}^\alpha \mathbf{a}_\alpha + q^3\mathbf{d} \tag{15}$$

respectively, where $n^{\beta\alpha} = \widetilde{n}^{\beta\alpha} + b^\beta_\gamma m^{\gamma\alpha}$, $q^\alpha = \tilde{q}^\alpha + b^3_\gamma m^{\gamma\alpha}$, and

$$\widetilde{n}^{\beta\alpha} = \int_{h_-}^{h_+} \sigma^{\beta\alpha} z\, d\theta, \qquad m^{\gamma\alpha} = \int_{h_-}^{h_+} \sigma^{\gamma\alpha}\theta z\, d\theta, \qquad \tilde{q}^\alpha = \int_{h_-}^{h_+} \sigma^{\alpha 3} z\, d\theta \tag{16}$$

Note that the effective membrane force tensor $\widetilde{n}^{\beta\alpha}$ as well as the bending moment tensor $m^{\beta\alpha}$ inherit their symmetry from the Cauchy stress tensor $\sigma^{\beta\alpha}$. Concluding, the virtual work of the internal forces reads

$$\delta W_{int} = \int \left[\delta\varepsilon_{\alpha\beta}\widetilde{n}^{\alpha\beta} + \delta\kappa_{\alpha\beta}m^{\alpha\beta} + \delta\gamma_\alpha \tilde{q}^\alpha\right] \sqrt{a}\, d\theta^1 d\theta^2 \tag{17}$$

Therein, the transverse normal force q^3 and the first order shear force $m^{3\alpha}$,

$$q^3 = \int_{h_-}^{h_+} \sigma^{33}\, z\, d\theta\,, \qquad m^{3\alpha} = \int_{h_-}^{h_+} \sigma^{3\alpha}\, \theta\, z\, d\theta \tag{18}$$

have dropped out. The first on due to $\delta E_{33} = 0$ and the second one due to $\mathbf{d}_{,\alpha} \cdot \mathbf{d} = 0$.

Confining the consideration to the simplest case, a Saint-Venant-Kirchhoff material law is applied. Accordingly, the constitutive equations read

$$\widetilde{n}^{ab} = Q^{abcd}\varepsilon_{cd}, \quad m^{ab} = \frac{t^3}{12}Q^{abcd}\kappa_{cd}, \quad \tilde{q}^a = t\,\alpha_s\,\mu\,\gamma_a \tag{19}$$

With Young's modulus E and Poisson ration ν, the plane-stress elasticity tensor and shear modulus read

$$Q^{abcd} = \frac{tE}{1-\nu^2}\left[\nu\delta^{ab}\delta^{cd} + (1-\nu)\delta^{ac}\delta^{bd}\right], \qquad \mu = \frac{E}{2\,(1+\nu)} \tag{20}$$

respectively. Finally, $\alpha_s = 5/6$ is the well-known shear correction factor.

2.3 Shell Kinematics Based on the Deformation Gradient

An alternative to the above derivations is due to [29], [26], [17]. Although this theory has been derived originally in a different way, here it is deduced analogously to the previous section starting from the variation of the strain energy in terms of the 1st Piola-Kirchhoff (PK1) stress tensor

$$\mathbf{P} = j\sigma^{ij}\mathbf{g}_i \otimes \mathbf{G}_j, \tag{21}$$

That is,

$$\delta W_{int} = \int_{\mathcal{B}_0} \delta\mathbf{F} : \mathbf{P}\, dV_0 \tag{22}$$

Introducing the traction vectors,

$$\mathbf{p}^\alpha = \mathbf{P}\mathbf{G}^\alpha = j\sigma^{i\alpha}\mathbf{g}_i, \qquad \mathbf{p}^3 = \mathbf{P}\mathbf{T}_3 = j\sigma^{i3}\mathbf{g}_i \tag{23}$$

The PK1 stress tensor can be written as,

$$\mathbf{P} = \mathbf{p}^{\alpha} \otimes \mathbf{G}_{\alpha} + \mathbf{p}^{3} \otimes \mathbf{D} \tag{24}$$

Analogously the variation of the deformation gradient reads

$$\delta\mathbf{F} = \delta\mathbf{g}_{\alpha} \otimes \mathbf{G}^{\alpha} + \delta\mathbf{d} \otimes \mathbf{D} \tag{25}$$

According to the Reissner-Mindlin kinematic assumption one can write

$$\mathbf{g}_{\alpha} = \boldsymbol{\phi}_{,\alpha} + \theta\, \mathbf{d}_{,\alpha}, \quad \mathbf{d} = \mathbf{Q}\mathbf{D} \tag{26}$$

where $\mathbf{Q}$ is a rotation tensor. Consequently,

$$\delta\mathbf{d} = \delta\mathbf{Q}\mathbf{Q}^{T}\mathbf{d} = \delta\boldsymbol{\vartheta} \times \mathbf{d} \tag{27}$$

Further, writing $\mathbf{D} = \mathbf{Q}_0\mathbf{e}_3$ with $\mathbf{e}_3$ being the global z direction one obtains

$$\mathbf{d}_{,\alpha} = \mathbf{Q}_{,a}\mathbf{D} + \mathbf{Q}\mathbf{D}_{,\alpha} = \mathbf{Q}_{,\alpha}\mathbf{Q}^{T}\mathbf{d} + \mathbf{Q}\mathbf{Q}_{0,\alpha}\mathbf{Q}_0^{T}\mathbf{Q}^{T}\mathbf{d} = (\boldsymbol{\omega}_{\alpha} + \boldsymbol{\omega}_{0\alpha}) \times \mathbf{d} \tag{28}$$

Note that $\delta\mathbf{Q}\mathbf{Q}^{T}$, $\mathbf{Q}_{,\alpha}\mathbf{Q}^{T}$, and $\mathbf{Q}_{0,\alpha}\mathbf{Q}_0^{T}$ are skew-symmetric tensors. The corresponding axial vectors are denoted by

$$\boldsymbol{\vartheta} = \mathrm{ad}^{-1}\left(\delta\mathbf{Q}\mathbf{Q}^{T}\right), \quad \boldsymbol{\omega}_{\alpha} = \mathrm{ad}^{-1}\left(\mathbf{Q}_{,\alpha}\mathbf{Q}^{T}\right), \quad \boldsymbol{\omega}_{0\alpha} = \mathrm{ad}^{-1}\left(\mathbf{Q}_{0,\alpha}\mathbf{Q}_0^{T}\right) \tag{29}$$

With the above definitions the variation of the natural basis vectors becomes,

$$\delta\mathbf{g}_{\alpha} = \delta\boldsymbol{\phi}_{,\alpha} + \theta(\delta\bar{\boldsymbol{\omega}}_{\alpha} \times \mathbf{d} + \bar{\boldsymbol{\omega}}_{\alpha} \times \delta\mathbf{d}) \tag{30}$$

From the permutability of the operations of variation and derivative the following expression can be derived,

$$\delta\boldsymbol{\vartheta}_{,\alpha} = \delta\bar{\boldsymbol{\omega}}_{\alpha} - \delta\boldsymbol{\vartheta} \times \bar{\boldsymbol{\omega}}_{\alpha} = \delta\boldsymbol{\omega}_{\alpha} - \delta\boldsymbol{\vartheta} \times \boldsymbol{\omega}_{\alpha} \tag{31}$$

Putting all together,

$$\delta\mathbf{F} : \mathbf{P} = \delta\mathbf{g}_{\alpha} \cdot \mathbf{p}^{\alpha} + \delta\mathbf{d} \cdot \mathbf{p}^{3} = \delta\boldsymbol{\phi}_{,\alpha} \cdot \mathbf{p}^{\alpha} + \underline{\delta\mathbf{d} \cdot \mathbf{p}^{3}} + \theta(\delta\boldsymbol{\vartheta}_{,\alpha} \times \mathbf{d}) \cdot \mathbf{p}^{\alpha} \tag{32}$$

The underlined term in Eq. (32) can be reformulated applying the balance of angular momentum, i.e. the symmetry of the σ_{ij} or, equivalently,

$$\mathbf{p}^{\alpha} \times \mathbf{g}^{\alpha} + \mathbf{p}^{3} \times \mathbf{a}_3 = \mathbf{0} \tag{33}$$

Doing so,

$$\delta\mathbf{F} : \mathbf{P} = (\delta\boldsymbol{\phi}_{,\alpha} - \delta\boldsymbol{\vartheta} \times \boldsymbol{\phi}_{,\alpha})\mathbf{p}^{\alpha} + \theta\delta\boldsymbol{\vartheta}_{,\alpha} \cdot (\mathbf{d} \times \mathbf{p}^{\alpha}) \tag{34}$$

Finally,

$$\delta W_{int} = \int \left[\delta\boldsymbol{\varepsilon}_{\alpha}\mathbf{n}^{\alpha} + \delta\boldsymbol{\kappa}_{\alpha} \cdot (\mathbf{d} \times \mathbf{m}^{\alpha})\right] \sqrt{A}\, d\theta^1 d\theta^2 \tag{35}$$

where the virtual strains and curvatures vectors,

$$\delta\boldsymbol{\varepsilon}_{\alpha} = \delta\boldsymbol{\phi}_{,\alpha} - \delta\boldsymbol{\vartheta} \times \boldsymbol{\phi}_{,\alpha}, \qquad \delta\boldsymbol{\kappa}_{\alpha} = \delta\boldsymbol{\vartheta}_{,\alpha} = \delta\boldsymbol{\omega}_{\alpha} - \delta\boldsymbol{\vartheta} \times \boldsymbol{\omega}_{\alpha} \tag{36}$$

and the resultant traction vectors,

$$\mathbf{n}^\alpha = \int_{h_-}^{h_+} \mathbf{p}^\alpha Z \, d\theta = j^0 \int_{h_-}^{h_+} \sigma^{i\alpha} \mathbf{g}_i z \, d\theta \ , \tag{37}$$

$$\mathbf{m}^\alpha = \int_{h_-}^{h_+} \mathbf{p}^\alpha Z \, \theta \, d\theta = j^0 \int_{h_-}^{h_+} \sigma^{i\alpha} \mathbf{g}_i \, z \, \theta \, d\theta \tag{38}$$

have been introduced. Here, $j^0 = \sqrt{a/A}$ and $Z = \sqrt{G/A}$ are the Jacobian determinants of the reference and undeformed shell reference surface, respectively. With the components of the stress resultants,

$$N^{\beta\alpha} = j^0 \int_{h_-}^{h_+} \sigma^{\gamma\alpha} z_\gamma^\beta \, z \, d\theta \, , \qquad Q^\alpha = j^0 \int_{h_-}^{h_+} \sigma^{3\alpha} \, z \, d\theta \ , \tag{39}$$

$$M^{\beta\alpha} = j^0 \int_{h_-}^{h_+} \sigma^{\gamma\alpha} z_\gamma^\beta \, z \, \theta \, d\theta \, , \qquad M^{3\alpha} = j^0 \int_{h_-}^{h_+} \sigma^{3\alpha} z \, \theta \ d\theta \tag{40}$$

one has

$$\mathbf{n}^\alpha = N^{\beta\alpha} \mathbf{a}_\beta + Q^\alpha \mathbf{d} \ , \qquad \mathbf{m}^\alpha = M^{\beta\alpha} \mathbf{a}_\beta + M^{3\alpha} \mathbf{d} \tag{41}$$

Defining the components of the virtual strain vectors with respect to the convected basis,

$$\delta \boldsymbol{\varepsilon}_\alpha = \delta \varepsilon_{\beta\alpha} \mathbf{a}^\beta + \delta \gamma_\alpha \mathbf{d}, \quad \delta \boldsymbol{\kappa}_\alpha = \delta \kappa_{\beta\alpha} \mathbf{d} \times \mathbf{a}^\beta + \delta \kappa_{3\alpha} \mathbf{d} \tag{42}$$

the virtual strain energy reads,

$$\delta W_{int} = \int \left[\delta \varepsilon_{\beta\alpha} N^{\beta\alpha} + \delta \kappa_{\beta\alpha} M^{\beta\alpha} + \delta \gamma_\alpha Q^\alpha \right] \sqrt{A} \, d\theta^1 d\theta^2 \tag{43}$$

Apparently, $M^{3\alpha}$ and $\kappa_{3\alpha}$ do not appear in the above expression.

2.4 Shell Kinematics Based on a Non-symmetric Biot-type Strain

It is instructive to consider a backward rotation to the undeformed configuration. Therefore two Cartesian coordinate systems are introduced; $\mathbf{T}_i = \mathbf{Q}_0 \mathbf{e}_i$ and $\mathbf{t}_i = \mathbf{Q} \mathbf{T}_i$ related to the undeformed and deformed configurations respectively. Further a Biot-type stress tensor is defined,

$$\mathbf{B} = \mathbf{Q}^T \mathbf{P} = B^{ij} \mathbf{T}_i \otimes \mathbf{T}_j \tag{44}$$

Accordingly the backward rotated resultant traction vectors are used

$$\mathbf{N}^a = \mathbf{Q}^T \mathbf{n}^a \quad \mathbf{M}^a = \mathbf{Q}^T \mathbf{m}^a \tag{45}$$

In this text, indices $a, b, \cdots$ generally denote Components with respect to a Cartesian basis and take the values 1 and 2 (to be distinguished from $\alpha, \beta, \ldots$ which denote components with respect to a curvilinear (natural) basis. The corresponding strain and curvature vectors are,

$$\mathbf{E}_a = \mathbf{Q}^T \boldsymbol{\phi}_{,a} - \mathbf{T}_a \ , \qquad \mathbf{K}_a = \mathbf{Q}^T \boldsymbol{\kappa}_a \tag{46}$$

It can be easily determined that

$$\delta \mathbf{E}_a = \mathbf{Q}^T \delta \boldsymbol{\varepsilon}_a \ , \qquad \delta \mathbf{K}^a = \mathbf{Q}^T \delta \boldsymbol{\kappa}_a \tag{47}$$

In view of the above the work of internal forces can be written as,

$$W_{int} = \int [\, \delta \mathbf{E}_a \cdot \mathbf{N}^a + \delta \mathbf{K}^a \cdot (\mathbf{D} \times \mathbf{M}^a) \,] \sqrt{A}\, d\theta^1 d\theta^2 \tag{48}$$

Introducing the strain and curvature components,

$$E_{ba} = \mathbf{T}_b \cdot \mathbf{E}_a = \mathbf{t}_b \cdot \boldsymbol{\phi}_{,a} - \delta_{ab}, \qquad E_{3a} = \mathbf{T}_3 \cdot \mathbf{E}_a = \mathbf{t}_3 \cdot \boldsymbol{\phi}_{,a} \tag{49}$$

$$K_{ba} = (\mathbf{T}_3 \times \mathbf{T}_b) = (\boldsymbol{\omega}_a \times \mathbf{t}_3) \cdot \mathbf{t}_b, \quad K_{3a} = (\mathbf{T}_3 \times \mathbf{K}_a) = \mathbf{t}_3 \cdot \boldsymbol{\omega}_a \tag{50}$$

the strain energy becomes

$$W_{int} = \int (E_{ba} N^{ba} + K_{ba} M^{ba} + E_{3a} Q^a) \sqrt{A}\, d\theta^1 d\theta^2 \tag{51}$$

Again, applying the plane-stress stiffness tensor,

$$Q^{abcd} = \frac{tE}{1-\nu^2} \left[\nu \delta^{ab} \delta^{cd} + (1-\nu) \delta^{ac} \delta^{bd} \right] \tag{52}$$

the constitutive relations are postulated according to

$$N^{(ab)} = Q^{abcd} E_{(cd)}, \quad N^{[ab]} = t\mu E_{[ab]} \tag{53}$$

$$M^{(ab)} = \frac{t^3}{12} Q^{abcd} K_{(cd)}, \quad M^{[ab]} = 0 \tag{54}$$

$$Q^a = t\, \alpha_s\, \mu\, E_{3a} \tag{55}$$

As usual, $(\cdot)_{(ab)}$ and $(\cdot)_{[ab]}$ denote symmetrization and anti-symmetrization, respectively.

2.5 Statically exact shell model

The shell theories described so far are ’non-exact’ in the sense that they rely on a kinematic assumption, namely Eq. (4). It leads to the fact that higher-order moments do not enter the virtual strain expression. According to an alternative approach due to [26], the stress resultants are defined as given in Eq. (38). The shell balance equation are then *exact* consequences of the three-dimensional balance equations. By postulating the existence of a strain energy

$$\delta W_{int} = \int [\delta \varepsilon_{\alpha\beta} N^{\beta\alpha} + \delta \kappa_{\beta\alpha} M^{\beta\alpha} + \delta \gamma_\alpha Q^\alpha + \delta \kappa_{3\alpha} M^{3\alpha}] \sqrt{A}\, d\theta^1 d\theta^2 \tag{56}$$

and applying the virtual work principle, the work-conjugate virtual strain measures are found again to be given by Eq. (36) and Eq. (42).

Due to the absence of kinematic restrictions, the $M^{3\alpha}$ enter the strain energy and $M^{\beta\alpha}$ is not necessarily symmetric. Therefore, a modified constitutive law is postulated [10],

$$N^{(ab)} = Q^{abcd} E_{(cd)}, \quad N^{[ab]} = t\mu E_{[ab]}, \tag{57}$$

$$M^{(ab)} = \frac{t^3}{12} Q^{abcd} K_{(cd)}, \quad M^{[ab]} = \frac{t^3}{12} \mu E_{[ab]} \tag{58}$$

$$Q^a = t\, \alpha_s\, \mu\, E_{3a}, \quad M^{3a} = \frac{t^3}{12}\, \beta_w\, \mu\, K_{3a} \tag{59}$$

$$\tag{60}$$

or, equivalantly,

$$N^{ab} = \bar{Q}^{abcd} E_{cd}, \qquad M^{ab} = \frac{t^3}{12}\, \bar{Q}^{abcd} K_{cd} \tag{61}$$

Both, α_s and β_w play the role of shear correction factors.

3 Methods for defining the drill rotation

In the turn of shell finite element formulations, two types of rotational quantities appear. The rotation tensor $\mathbf{R}$ represents the rigid body rotation according to the translational deformation field. Based on polar decomposition theorem, $\mathbf{F} = \mathbf{R}\mathbf{U}$ where $\mathbf{F}$ is the deformation gradient and $\mathbf{U}$ the right stretch tensor. In addition, it can be advantageous to introduce an *a priori* independent rotation tensor field $\mathbf{Q}$. When dealing with non polar materials, the two tensor fields $\mathbf{Q}$ and $\mathbf{R}$ are expected to coincide, $\mathbf{Q} = \mathbf{R}$. Since $\mathbf{U}$ is symmetric the following relation holds

$$\operatorname{skew}(\mathbf{Q}^T\mathbf{F}) = \mathbf{0} \qquad \text{or, equivalently,} \qquad \epsilon^{ijk}\mathbf{A}_j^T\mathbf{Q}^T\mathbf{F}\mathbf{A}_k = 0 \tag{62}$$

where the deformation gradient of the shell mid surface reads,

$$\mathbf{F} = \mathbf{a}_\alpha \otimes \mathbf{A}^\alpha + \mathbf{d} \otimes \mathbf{T}_3 + \mathcal{O}(\theta) \tag{63}$$

In Eq. (62), use has been made of the totally antisymmetric tensor ϵ^{ijk}. In the sequel three different approaches to deal with the indeterminacy of the drill rotation are presented. All of these methods provide a definition for the drill rotation through an appropriately defined constraint equation. Their differences as well as similarities are discussed.

3.1 The Approach of Fox & Simo [14]

Let the following modified quantities be defined as,

$$\widetilde{\mathbf{F}} = \widetilde{\mathbf{a}}_\alpha \otimes \mathbf{A}^\alpha + \mathbf{d} \otimes \mathbf{T}_3, \quad \widetilde{\mathbf{Q}} = \exp(\omega\widetilde{\mathbf{T}}_3) \tag{64}$$

where $\widetilde{\mathbf{T}}_3$ defines the skew-symmetric matrix and

$$\widetilde{\mathbf{a}}_\alpha = \widetilde{\mathbf{F}}\mathbf{A}_\alpha = \mathbf{a}_\alpha - (\mathbf{T}_3 \cdot \mathbf{a}_\alpha)\mathbf{T}_3 \tag{65}$$

is the projection of $\mathbf{a}_\beta$ onto the plane normal to the vector $\mathbf{T}_3$. In view of the above the drill rotation constraint equation can be written as follows,

$$\epsilon^{\alpha\beta}\mathbf{A}_\alpha\widetilde{\mathbf{Q}}^T\widetilde{\mathbf{F}}\mathbf{A}_\beta = \epsilon^{\alpha\beta}\mathbf{A}_\alpha\widetilde{\mathbf{Q}}^T\widetilde{\mathbf{a}}_\beta \overset{!}{=} 0 \tag{66}$$

where $\epsilon^{\alpha\beta}$ is the antisymmetric permutation symbol. With

$$\widetilde{\mathbf{u}}_{,\alpha} = \mathbf{u}_{,\alpha} - (\mathbf{T}_3 \cdot \mathbf{u}_{,\alpha})\mathbf{T}_3 = u^\beta|_\alpha\mathbf{A}_\beta \tag{67}$$

one obtains

$$\widetilde{\mathbf{a}}_\alpha = \mathbf{A}_\alpha + \widetilde{\mathbf{u}}_{,\alpha} = \mathbf{A}_\beta(\delta_\alpha^\beta + u^\beta|_\alpha) \tag{68}$$

Substituting Eq. (68) into Eq. (66),

$$\epsilon^{\alpha\beta}\mathbf{A}_\alpha\widetilde{\mathbf{Q}}^T\mathbf{A}_\gamma(\delta_\alpha^\gamma + u^\gamma|_\alpha) \overset{!}{=} 0 \tag{69}$$

The product $\mathbf{A}_\alpha\widetilde{\mathbf{Q}}^T\mathbf{A}_\gamma$ defines the components of the rotation tensor $\widetilde{Q}_{\gamma\alpha}$ which can be written as,

$$\widetilde{Q}_{\gamma\alpha} = A_{\alpha\gamma}\cos\omega + \sqrt{A}\,\epsilon_{\alpha\gamma}\sin\omega \tag{70}$$

Substituting Eq. (70) into Eq. (66) and after some simplifications the drill rotation constraint is derived to be,

$$(u_1|_2 - u_2|_1)\cos\omega + \sqrt{A}(2 + u^1|_1 + u^2|_2)\sin\omega \overset{!}{=} 0 \tag{71}$$

A drawback of the above described method is that the left hand side of Eq. (71) depends on the length of the tangent vectors. In the context of finite element implementation it therefore leads to an unacceptable mesh dependence. As a remedy, one should use the Cartesian basis vectors $\mathbf{T}_\alpha$ instead of the natural basis vectors $\mathbf{A}_\alpha$. The corresponding drill rotation constraint equation is then derived from

$$\epsilon^{ab}\mathbf{T}_a\widetilde{\mathbf{Q}}^T\widetilde{\mathbf{F}}\mathbf{T}_b = 0 \tag{72}$$

3.2 The Modification of Rebel [25]

In an attempt to alleviate the problem with the length dependencies of the covariant derivatives, a modification of the above method was proposed by Rebel [25]. Here, the rotation tensor $\mathbf{Q}$ is split into two parts; the first corresponds to out of plane rotation while the second to in-plane rotation. Thus one can write,

$$\mathbf{Q} = \mathbf{Q}_d\boldsymbol{\Lambda}, \qquad \mathbf{Q}_d = \exp(\omega\widetilde{\mathbf{d}}), \qquad \mathbf{d} = \boldsymbol{\Lambda}\mathbf{T}_3 \tag{73}$$

With the above the rotation constraint equation reads,

$$\epsilon^{\alpha\beta}\mathbf{A}_\alpha^T\mathbf{Q}^T\widetilde{\mathbf{F}}\mathbf{A}_\beta = \epsilon^{\alpha\beta}\mathbf{A}_\alpha^T\boldsymbol{\Lambda}^T\mathbf{Q}_d^T\widetilde{\mathbf{a}}_\beta \overset{!}{=} 0 \ , \tag{74}$$

where

$$\widetilde{\mathbf{a}}_\beta = \mathbf{a}_\beta - (\mathbf{d}\cdot\mathbf{a}_\beta)\,\mathbf{d} \tag{75}$$

is the projection of $\mathbf{a}_\beta$ onto the plane normal to the director $\mathbf{d}$ and the modified deformation gradient $\widetilde{\mathbf{F}}$ is defined accordingly. Note that the rotated basis vectors $\boldsymbol{\Lambda}\mathbf{A}_\alpha$ lie in the same plane. In order to avoid the dependency on the length of the deformed basis, as discussed previously, a normalization is introduced. That is,

$$\epsilon^{\alpha\beta}\frac{\mathbf{A}_\alpha^T}{\|\mathbf{A}_\alpha^T\|}\mathbf{Q}^T\frac{\widetilde{\mathbf{a}}_\beta}{\|\widetilde{\mathbf{a}}_\beta\|} = 0 \tag{76}$$

Alternatively, to avoid this artificial normalization procedure it would be beneficial to use the Cartesian basis vectors $\mathbf{T}_a$ instead of $\mathbf{A}_\alpha$. Note that here the drill rotation is defined as the rotation about the director vector unlike the approach of [14] where the drill rotation is defined as the rotation around the direction normal to the tangent plane of the mid surface.

3.3 The approach of Wisniewski & Turska [38]

The third and last alternative to treat the drill rotation in the context of shells, is due to Wiesniwski & Turska [38]. Here the rotation tensor is split into two parts,

$$\mathbf{Q}_0 = \mathbf{Q}_t\boldsymbol{\Lambda}_0, \qquad \mathbf{Q}_t = \exp(\omega\widetilde{\mathbf{t}}_3), \qquad \mathbf{t}_3 = \boldsymbol{\Lambda}_0\mathbf{T}_3 \tag{77}$$

where $\mathbf{Q}_t$ corresponds to the drill rotation and $\boldsymbol{\Lambda}_0$ is the director orienting rotation. With the above definitions the rotation constraint equation becomes,

$$\epsilon^{ab}\mathbf{T}_a^T\mathbf{Q}_0^T\mathbf{F}_0\mathbf{T}_b^T = \epsilon^{ab}\mathbf{T}_a^T\boldsymbol{\Lambda}_0^T\mathbf{Q}_t^T\boldsymbol{\phi}_{,b} = 0 \tag{78}$$

Since $\boldsymbol{\phi}_{,b}$ lies in the pane spanned by the vectors $\breve{\mathbf{T}}_a$, one can substitute in the above the following expression, $\boldsymbol{\phi}_{,b} = \breve{\mathbf{T}}_c^T\boldsymbol{\phi}_{,b}\breve{\mathbf{T}}_c$. Then,

$$\epsilon^{ab}\breve{\mathbf{T}}_a\mathbf{Q}_t^T\breve{\mathbf{T}}_c^T\boldsymbol{\phi}_{,b}\breve{\mathbf{T}}_c = \epsilon^{ab}Q_{ac}\boldsymbol{\phi}_{,b}\breve{\mathbf{T}}_c = 0 \tag{79}$$

Using $\mathbf{t}_\alpha = Q_{ac}\breve{\mathbf{T}}_c$ the above is written,

$$\epsilon^{ab}(\mathbf{t}_a \cdot \boldsymbol{\phi}_{,b}) = 0 \tag{80}$$

The above can be written with respect to the displacement gradients as follows,

$$(u_{1,2} - u_{2,1})\cos\omega + (2 + u_{1,1} + u_{2,2})\sin\omega = 0 \tag{81}$$

3.4 Comparison of RC with Micropolar Approach

All the above described methods attempt to provide a definition for the drill rotation in terms of a constraint equation. In the following the relation of the above methods with the definition of the drill rotation obtained from the shell theory in Subsection 2.4 is presented here.

$$\delta\mathbf{F} : \mathbf{P} = (\mathbf{Q}^T\delta\mathbf{F}) : (\mathbf{Q}^T\mathbf{P}) = \delta(\mathbf{Q}^T\mathbf{F}) : \mathbf{Q}^T\mathbf{P} - \underline{(\mathbf{Q}^T\mathbf{F}) : (\mathbf{Q}^T\mathbf{P})} \tag{82}$$

The underlined term vanishes since,

$$(\delta\mathbf{Q}^T\mathbf{F}) : (\mathbf{Q}^T\mathbf{P}) = \mathbf{F} : (\delta\mathbf{Q}\mathbf{Q}^T\mathbf{P}) = \mathrm{tr}(\delta\tilde{\boldsymbol{\vartheta}}\mathbf{P}\mathbf{F}^T) = 0 \tag{83}$$

With the help of the above and introducing the Biot-type strain tensor $\mathbf{H} = \mathbf{Q}^T\mathbf{F}$ Eq. (82) can be written as follows

$$\delta\mathbf{F} : \mathbf{P} = \delta\mathbf{H} : \mathbf{B} = \delta\mathbf{H}_s : \mathbf{B}_s + \delta\,\mathrm{skew}(\mathbf{Q}^T\mathbf{F}) : \mathbf{B}_a\,, \tag{84}$$

where the subscripts s, a denote the symmetric and antisymetric part. The integral of the antisymmetric part is calculated to be,

$$\int \delta\,\mathrm{skew}(\mathbf{Q}^T\mathbf{F}) : \mathbf{B}\; dV = \int [\delta E_{[ab]}N_{[ab]} + \delta K_{[ab]}M_{[ab]} + \delta E_{3a}N_{3a}]\; dA \tag{85}$$

$$= \int [t\mu(\delta E_{[ab]}E_{[ab]}) + \frac{t^3}{12}\mu\delta K_{[ab]}K_{[ab]} + t\mu\delta E_{3a}E_{3a}]\; dA\,, \tag{86}$$

where

$$E_{[ab]} = \mathbf{t}_1 \cdot \boldsymbol{\phi}_{,2} - \mathbf{t}_2 \cdot \boldsymbol{\phi}_{,1} = (\mathbf{t}_1 \cdot \boldsymbol{\phi}_{,1} + \mathbf{t}_2 \cdot \boldsymbol{\phi}_{,2})\tan\omega_d \tag{87}$$

$$K_{[ab]} = \mathbf{t}_1 \cdot \mathbf{t}_{3,2} - \mathbf{t}_2 \cdot \mathbf{t}_{3,1} = (\mathbf{t}_1 \cdot \boldsymbol{\phi}_{,1} + \mathbf{t}_2 \cdot \boldsymbol{\phi}_{,2})\tan\omega_t \tag{88}$$

It turns out that this result corresponds to a linear dependence of the drill rotation on the thickness coordinate θ. That is [38],

$$\omega = \omega_d + \theta\omega_t, \tag{89}$$

where ω_t is the in-plane twist rotation and ω_d is the drill rotation at the reference surface. Enforcing the rotation constraint equation Eq. (80) according to Section 5, a direct equivalence with the first term in Eq. (86) can be established.

4 Finite Element Discretizations

4.1 Linear Flat 4-Node Shell (LFS4) Element

The position vector $\boldsymbol{\Phi}$ and director vector $\mathbf{D}$ on the flattened shell reference surface at the initial configuration can be interpolated as follows,

$$\boldsymbol{\Phi}^h = \sum_{I=1}^{4} N_I \boldsymbol{\Phi}_I, \quad \mathbf{D}^h = \sum_{I=1}^{4} N_I \mathbf{D}_I, \tag{90}$$

where $\boldsymbol{\Phi}_I$ are the position vectors of the nodes in the global coordinate system and $\mathbf{D}_I = \mathbf{a}_{3I}$ are the nodal shell directors which are perpendicular to the shell mid surface. Note that the superscript h denotes the finite element approximation and shall be used throughout this thesis. The bi-linear shape functions N_I are defined by,

$$N_I = \frac{1}{4}(1 + \xi_I^1 \xi^1)(1 + \xi_I^2 \xi^2), \tag{91}$$

where the ξ^α are the *natural coordinates* which belong to the bi-unit square domain spanned by the coordinates of the corner nodes $\{\xi_I^1, \xi_I^2\} = \{\mp 1, \mp 1\}$. For computational reasons, an additional orthogonal basis $(\mathbf{T}_i)$ is introduced at the element center. The length-measuring coordinates associated with the in-plane basis vectors $\mathbf{T}_a$ are denoted with s^a, where $a = 1, 2$. The derivatives of the interpolated position vector and director vectors with respect to s_a coordinates can be determined as follows,

$$\boldsymbol{\Phi}^h_{,a} = \sum_{I=1}^{4} N_{I,a} \boldsymbol{\Phi}_I, \quad \mathbf{D}^h_{,a} = \mathbf{0} \tag{92}$$

Analogous to Eq. (90), the displacements and rotations can be interpolated using the bi-linear interpolation functions as,

$$\mathbf{u}^h = \sum_{I=1}^{4} N_I \mathbf{u}_I, \quad \boldsymbol{\vartheta}^h = \sum_{I=1}^{4} N_I \boldsymbol{\vartheta}_I \tag{93}$$

where $\mathbf{u}_I = u_{Ik}\mathbf{e}_k$ is the nodal displacement vector and $\boldsymbol{\vartheta}$ the rotation vector. In order to avoid shear locking, the transverse shear components are interpolated according to the concept of Assumed Natural Strains (ANS) [12].

4.2 Enhancement of the membrane strains

The method of *Enhanced Assumed Strains* (EAS) was initiated by [35] for the linear case and by [30], [31] for the non linear case. The theory is based on the idea to add to the compatible strain field an incompatible enhanced strain field as,

$$\boldsymbol{\varepsilon} = \boldsymbol{\varepsilon}^h + \tilde{\boldsymbol{\varepsilon}}, \tag{94}$$

where the compatible strains are calculated by,

$$\boldsymbol{\varepsilon}^h = \sum_{I=1}^{4} \mathbf{B}_I \hat{\mathbf{u}}_I, \quad \hat{\mathbf{u}}_I = [\mathbf{u}_I, \boldsymbol{\vartheta}_I]^T, \tag{95}$$

with $\mathbf{B}$ being the strain-displacement matrix. In addition, the enhanced strains components are determined as [35],

$$\tilde{\boldsymbol{\varepsilon}} = \frac{j_0}{j} \mathbf{J}_0 \mathbf{M}\, \boldsymbol{\alpha}_e, \tag{96}$$

Here, the membrane strain components ε_{ab} are organized in a vector format,

$$\boldsymbol{\varepsilon} = [\varepsilon_{11}\ \varepsilon_{22}\ 2\varepsilon_{12}]^T \tag{97}$$

The 3×3 matrix $\mathbf{J}_0$ transforms the strain components from the skew basis $(\mathbf{A}^\alpha)$ at the element center to the Cartesian basis $(\mathbf{T}^a)$ according to

$$\tilde{\varepsilon}_{ab} = J_a{}^\alpha\, J_b{}^\beta\, \tilde{\varepsilon}_{\alpha\beta}, \quad \Leftrightarrow \quad \tilde{\boldsymbol{\varepsilon}}^{(T)} = \mathbf{J}_0\, \tilde{\boldsymbol{\varepsilon}}^{(A)} \tag{98}$$

where

$$\mathbf{J}_0 = \begin{bmatrix} (J_1{}^1)^2 & (J_1{}^2)^2 & J_1{}^1\, J_1{}^2 \\ (J_2{}^1)^2 & (J_2{}^2)^2 & J_2{}^1\, J_2{}^2 \\ 2\, J_1{}^1\, J_2{}^1 & 2\, J_1{}^2\, J_2{}^2 & J_1{}^1\, J_2{}^2 + J_2{}^1\, J_1{}^2 \end{bmatrix}, \qquad J_a{}^\alpha = \mathbf{T}_a \cdot \mathbf{A}^\alpha \tag{99}$$

The matrix $\mathbf{M}$ defines the enhanced strain modes. According to [2],

$$\mathbf{M}^{(7)} = \begin{bmatrix} \xi^1 & 0 & 0 & 0 & \xi^1\xi^2 & 0 & 0 \\ 0 & \xi^2 & 0 & 0 & 0 & \xi^1\xi^2 & 0 \\ 0 & 0 & \xi^1 & \xi^2 & 0 & 0 & \xi^1\xi^2 \end{bmatrix} \tag{100}$$

The amplitudes of these 7 modes are stored in the vector $\boldsymbol{\alpha}_e$.

In the case of the micropolar formulation, the strain tensor is nonsymmetric, thus

$$\boldsymbol{\varepsilon} = [\varepsilon_{11}\ \varepsilon_{22}\ \varepsilon_{12}\ \varepsilon_{21}]^T \tag{101}$$

For the transformation, a 4×4 matrix $\mathbf{J}_0^{4\times4}$ instead of the $\mathbf{J}_0$ has to be applied,

$$\mathbf{J}_0^{(4\times4)} = \begin{bmatrix} (J_1{}^1)^2 & (J_1{}^2)^2 & J_1{}^1\, J_1{}^2 & J_1{}^2\, J_1{}^1 \\ (J_2{}^1)^2 & (J_2{}^2)^2 & J_2{}^1\, J_2{}^2 & J_2{}^2\, J_2{}^1 \\ J_1{}^1\, J_2{}^1 & J_1{}^2\, J_2{}^2 & J_1{}^1\, J_2{}^2 & J_1{}^2\, J_2{}^1 \\ J_2{}^1\, J_1{}^1 & J_2{}^2\, J_1{}^2 & J_2{}^1\, J_1{}^2 & J_2{}^2\, J_1{}^1 \end{bmatrix} \tag{102}$$

The 8 strain modes are defined according to [10],

$$\mathbf{M}^{(8)} = \begin{bmatrix} \xi^1 & 0 & 0 & 0 & \xi^1\xi^2 & 0 & 0 & 0 \\ 0 & \xi^2 & 0 & 0 & 0 & \xi^1\xi^2 & 0 & 0 \\ 0 & 0 & \xi^1 & 0 & 0 & 0 & \xi^1\xi^2 & 0 \\ 0 & 0 & 0 & \xi^2 & 0 & 0 & 0 & \xi^1\xi^2 \end{bmatrix} \tag{103}$$

4.3 Enhancement of the drill rotation constraint

The implementations based on a splitting of the strain tensor in a symmetric and an antisymmetric part, $\varepsilon_{(ab)}$ and $\varepsilon_{[ab]}$, respectively, lead to the method of the *enhanced rotation constraint.* Therefore, the strain vector format

$$\underline{\tilde{\varepsilon}} = \left[\varepsilon_{11}\ \varepsilon_{22}\ 2\varepsilon_{(12)}\ 2\varepsilon_{[12]}\right]^T \tag{104}$$

is adopted. The correspoinding transformation matrix is denoted by $\bar{\mathbf{J}}_0^{(4\times4)}$. Two different sets of enhanced strain modes are considered,

$$\mathbf{M}^{(8_1)} = \begin{bmatrix} \xi^1 & 0 & 0 & 0 & \xi^1\xi^2 & 0 & 0 & 0 \\ 0 & \xi^2 & 0 & 0 & 0 & \xi^1\xi^2 & 0 & 0 \\ 0 & 0 & \xi^1 & \xi^2 & 0 & 0 & \xi^1\xi^2 & 0 \\ 0 & 0 & 0 & 0 & 0 & 0 & 0 & \xi^1\xi^2 \end{bmatrix} \tag{105}$$

and

$$\mathbf{M}^{(8_2)} = \begin{bmatrix} \xi^1 & 0 & 0 & 0 & \xi^1\xi^2 & 0 & 0 & 0 \\ 0 & \xi^2 & 0 & 0 & 0 & \xi^1\xi^2 & 0 & 0 \\ 0 & 0 & \xi^1 & \xi^2 & 0 & 0 & \xi^1\xi^2 & 0 \\ 0 & 0 & \xi^1 & -\xi^2 & 0 & 0 & 0 & \xi^1\xi^2 \end{bmatrix} \tag{106}$$

leading to the implementations termed 'ERC$_1$' and 'ERC$_2$'. Finally, the method which turns out to perform best applies the enhanced strain modes according to Eq. (103) and a transformation of the kind

$$\begin{bmatrix} \varepsilon_{11} \\ \varepsilon_{22} \\ 2\varepsilon_{(12)} \\ 2\varepsilon_{[12]} \end{bmatrix}^{(T)} = \bar{\bar{\mathbf{J}}}_0^{(4\times4)} \begin{bmatrix} \varepsilon_{11} \\ \varepsilon_{22} \\ \varepsilon_{12} \\ \varepsilon_{21} \end{bmatrix}^{(A)} \tag{107}$$

The corresponding implementation is simply termed 'ERC'.

4.4 Variational formulation

Basis for the linear finite element formulation is the modified Hu-Washizu variational principle

$$\begin{aligned} \int \Big[& t\, Q^{abcd} \left(\varepsilon_{ab} + \tilde{\varepsilon}_{ab}\right) \left(\delta\varepsilon_{cd} + \delta\tilde{\varepsilon}_{cd}\right) + \frac{t^3}{12}\, Q^{abcd} \kappa_{ab} \delta\kappa_{cd} + \alpha_s\, t\, \mu\, \gamma_a \delta\gamma_a \\ & + \beta\, t\, \mu\, c\, \delta c \Big] \sqrt{A}\, d\theta^1 d\theta^2 = \delta W_{ext} \end{aligned} \tag{108}$$

where $c = E_{[12]}$ refers to the drill rotation constraint, Section 5, and δW_{ext} is the virtual work of the external forces.

For the micropolar formulation,

$$\begin{aligned} \int \Big[& t\, \bar{Q}^{abcd} \left(E_{ab} + \tilde{\varepsilon}_{ab}\right) \left(\delta E_{cd} + \delta\tilde{\varepsilon}_{cd}\right) + \frac{t^3}{12}\, \bar{Q}^{abcd} K_{ab} \delta K_{cd} \\ & + \alpha_s\, t\, \mu\, E_{3a} \delta E_{3a} + \beta_w\, \frac{t^3}{12}\, \mu\, K_{3a} \delta K_{3a} \Big] \sqrt{A}\, d\theta^1 d\theta^2 = \delta W_{ext} \end{aligned} \tag{109}$$

Finally, for the enhanced rotation constraint

$$\begin{aligned} \int \Big[& t\, Q^{abcd} \left(E_{(ab)} + \tilde{\varepsilon}_{(ab)}\right) \left(\delta E_{(cd)} + \delta\tilde{\varepsilon}_{(cd)}\right) + \frac{t^3}{12}\, Q^{abcd} K_{(ab)} \delta K_{(cd)} \\ & + \beta\, t\, \mu\, \left(E_{[12]} + \tilde{\varepsilon}_{[12]}\right) \left(\delta E_{[12]} + \delta\tilde{\varepsilon}_{[12]}\right) + \beta_t\, \frac{t^3}{12}\, \mu\, K_{[12]} \delta K_{[12]} \\ & + \alpha_s\, t\, \mu\, E_{3a} \delta E_{3a} + \beta_w\, \frac{t^3}{12}\, \mu\, K_{3a} \delta K_{3a} \Big] \sqrt{A}\, d\theta^1 d\theta^2 = \delta W_{ext} \end{aligned} \tag{110}$$

4.5 Allman Shape Functions

Within the context of Allman shape function the discretized displacement vector is modified as follows,

$$\mathbf{u} = \sum_{I=1}^{4} N_I \mathbf{u}_I + \sum_{H=5}^{8} N_H \Delta\mathbf{u}_H \,, \tag{111}$$

where the hierarchical shape functions N_H are defined as follows,

$$N_5 = \frac{1}{2}(1-(\xi^1)^2)(1-\xi^2), \qquad N_7 = \frac{1}{2}(1-(\xi^1)^2)(1+\xi^2) \tag{112}$$

$$N_6 = \frac{1}{2}(1-(\xi^2)^2)(1+\xi^1), \qquad N_8 = \frac{1}{2}(1-(\xi^2)^2)(1-\xi^2) \tag{113}$$

The hierarchical displacement vectors, $\Delta\mathbf{u}_H$, at the mid-points of the element boundaries are given by,

$$\Delta\mathbf{u}_H = -\frac{L_{JK}}{8}(\omega_K - \omega_J)\mathbf{n}_{JK}, \quad H = 5,6,7,8 \tag{114}$$

with $J = H - 4$, $K = \mathrm{mod}(H,4) + 1$ and L_{JK} is the length of the boundary JK and $\mathbf{n}_{JK}$ is the vector normal to the initial element boundary.

5 Implementation of drill RC equation

The linearisation of the drill RC equation reads,

$$c = \omega + \frac{1}{2}(u_{1,2} - u_{2,1}) = 0 \tag{115}$$

Eq. (115) can be formulated as an integral (i.e. weak) form and therefore be added in any variational principle. Using a penalty method the extended functional Π^* reads,

$$\Pi^*(\mathbf{u}, \boldsymbol{\sigma}, \mathbf{Q}) = \Pi(\mathbf{u}, \boldsymbol{\sigma}) + \Pi^P_{RC}, \tag{116}$$

where the penalty functional Π_{RC} is given as [37],

$$\Pi^P_{RC} = \int_{\mathcal{B}} F^P_{RC}(\mathbf{u}, \mathbf{Q}) \, dV, \quad F^P_{RC}(\mathbf{u}, \mathbf{Q}) = \frac{\gamma}{2} c^2, \tag{117}$$

The linearisation of the penalty functional Π_{RC} yields to the following equations

$$\left(\mathbf{K} + \gamma \begin{bmatrix} \mathbf{K}^{RC}_{uu} & \mathbf{K}^{RC}_{u\vartheta} \\ \mathbf{K}^{RC}_{\vartheta u} & \mathbf{K}^{RC}_{\vartheta\vartheta} \end{bmatrix}\right) \begin{bmatrix} \Delta\mathbf{u} \\ \Delta\boldsymbol{\vartheta} \end{bmatrix} = -\begin{Bmatrix} \mathbf{r} + \gamma\mathbf{r}_u \\ \gamma\mathbf{r}_\vartheta \end{Bmatrix}, \tag{118}$$

where $\mathbf{r}_u, \mathbf{r}_\vartheta$ are the residuals. Here, $\mathbf{u} = [u^i_I] = [u^1_1 \; u^2_1 \; u^3_1 \; \cdots \; u^1_4 \; u^2_4 \; u^3_4]$ is the element displacement vector and $\boldsymbol{\vartheta} = [\vartheta^i_I] = [\vartheta^1_1 \; \vartheta^2_1 \; \vartheta^3_1 \; \cdots \; \vartheta^1_4 \; \vartheta^2_4 \; \vartheta^3_4]$ is the rotation vector while $\Delta\mathbf{u}, \Delta\boldsymbol{\vartheta}$ are the incremental vectors. Note that I, i denote the node number and component with respect to the global coordinate system $\mathbf{e}_i$ respectively. When $\mathbf{u} = \mathbf{0}$ and $\boldsymbol{\vartheta} = \mathbf{0}$, it follows that $\mathbf{r}_u = \mathbf{0}, \mathbf{r}_\vartheta = \mathbf{0}$ and $\mathbf{r} = -\mathbf{f}$. Hence Eq. (118) reduces to,

$$\left(\mathbf{K} + \gamma \begin{bmatrix} \mathbf{K}^{RC}_{uu} & \mathbf{K}^{RC}_{u\vartheta} \\ \mathbf{K}^{RC}_{\vartheta u} & \mathbf{K}^{RC}_{\vartheta\vartheta} \end{bmatrix}\right) \begin{bmatrix} \Delta\mathbf{u} \\ \Delta\boldsymbol{\vartheta} \end{bmatrix} = \begin{bmatrix} \mathbf{f} \\ \mathbf{0} \end{bmatrix}, \tag{119}$$

where $\mathbf{f}$ is the vector of external loads. Introducing the following notation,

$$\frac{\partial(\cdot)}{\partial \mathbf{u}} = \left[\frac{\partial(\cdot)}{\partial u_I^i}\right]_{I,i=1,2,3}, \qquad \frac{\partial(\cdot)}{\partial \boldsymbol{\vartheta}} = \left[\frac{\partial(\cdot)}{\partial \vartheta_I^i}\right]_{I,i=1,2,3} \tag{120}$$

the residuals of Eq. (118) are defined by,

$$\mathbf{r}_u = \frac{\partial \Pi_{RC}^P}{\partial \mathbf{u}}, \ \frac{\partial \Pi_{RC}^P}{\partial u_I^i} = \int_{\mathcal{B}} \frac{\partial F_{RC}^P}{\partial u_I^i}\, dV, \quad \mathbf{r}_\vartheta = \frac{\partial \Pi_{RC}^P}{\partial \boldsymbol{\vartheta}}, \ \frac{\partial \Pi_{RC}^P}{\partial \vartheta_I^i} = \int_{\mathcal{B}} \frac{\partial F_{RC}^P}{\partial \vartheta_I^i}\, dV \tag{121}$$

and the stiffness matrices,

$$\begin{aligned} \boldsymbol{K}_{uu}^{RC} &= \frac{\partial \mathbf{r}_u}{\partial \mathbf{u}}, \ \frac{\partial \mathbf{r}_u}{\partial u_J^j} = \int_{\mathcal{B}} \frac{\partial^2 F_{RC}^P}{\partial u_J^j \partial u_I^i}\, dV, \quad & \boldsymbol{K}_{u\vartheta}^{RC} &= \frac{\partial \mathbf{r}_u}{\partial \boldsymbol{\vartheta}}, \ \frac{\partial \mathbf{r}_u}{\partial \vartheta_J^j} = \int_{\mathcal{B}} \frac{\partial^2 F_{RC}^P}{\partial \vartheta_J^j \partial u_I^i}\, dV \\ \boldsymbol{K}_{\vartheta u}^{RC} &= \frac{\partial \mathbf{r}_\vartheta}{\partial \mathbf{u}}, \ \frac{\partial \mathbf{r}_\vartheta}{\partial u_J^j} = \int_{\mathcal{B}} \frac{\partial^2 F_{RC}^P}{\partial u_J^j \partial \vartheta_I^i}\, dV, \quad & \boldsymbol{K}_{\vartheta\vartheta}^{RC} &= \frac{\partial \boldsymbol{r}_\vartheta}{\partial \boldsymbol{\vartheta}}, \ \frac{\partial \mathbf{r}_\vartheta}{\partial \vartheta_J^j} = \int_{\mathcal{B}} \frac{\partial^2 F_{RC}^P}{\partial \vartheta_J^j \partial \vartheta_I^i}\, dV \end{aligned} \tag{122}$$

In the sequel two different methods for the implementation of the dril RC constraint in the context of four-node shell elements are presented. In the first the area integration is performed analytically while in the second a two point Gauss quadrature is employed.

5.1 Analytical Integration Based on Taylor Series Expansion

Using Taylor series expansion for Eq. (115) at the element centre (i.e. $\xi^1 = \xi^2 = 0$) yields,

$$\bar{c}(\xi^1, \xi^2) = c|_0 + c_{,\xi^1}|_0 \xi^1 + c_{,\xi^2}|_0 \xi^2, \tag{123}$$

where here $|_0$ denotes quantities evaluated at the element center. Displacements and drill rotations are interpolated using the bilinear shape functions $N_I(\xi^1, \xi^2)$. For the sake of completeness these relations are repeated here,

$$\mathbf{u} = \sum_{I=1}^{4} N_I(\xi^1, \xi^2)\mathbf{u}_I, \quad \boldsymbol{\vartheta} = \sum_{I=1}^{4} N_I(\xi^1, \xi^2)\boldsymbol{\vartheta}_I \tag{124}$$

The derivatives of the displacement components at Eq. (115) are determined as follows

$$u_{b,\alpha} = J_{\alpha\beta}^{-1} \frac{\partial u_b}{\partial \xi^\beta} = J_{\alpha\beta}^{-1} \sum_{I=1}^{4} N_{,\xi^\beta}(\mathbf{t}_b \cdot \mathbf{e}_i) u_I^i \ , \tag{125}$$

where u_I^i are the displacement components i of the node I with respect to the global coordinate system $(\mathbf{e}_i)$. Substituting Eq. (124) and Eq. (125) into Eq. (115) with $\omega_I = \mathbf{t}_3 \cdot \boldsymbol{\vartheta}_I$ yields,

$$c(\xi^1, \xi^2) = \sum_{I=1}^{4} N_I(\mathbf{t}_3 \cdot \boldsymbol{\vartheta}_I) + \frac{1}{2}\left(J_{2\beta}^{-1} \sum_{I=1}^{4} N_{,\xi^\beta}(\mathbf{t}_1 \cdot \mathbf{e}_i) u_I^i - J_{1\beta}^{-1} \sum_{I=1}^{4} N_{,\xi^\beta}(\mathbf{t}_2 \cdot \mathbf{e}_i) u_I^i\right) \tag{126}$$

With the help of Eq. (126), the three terms of Eq. (123) can be determined as follows,

$$\begin{aligned}
c|_0 &= \frac{1}{4}\sum_{I=1}^{4}(\mathbf{t}_3\cdot\boldsymbol{\vartheta}_I) + \frac{1}{8}\left(J^{-1}_{2\beta}\sum_{I=1}^{4}\xi^{\beta}_{I}(\mathbf{t}_1\cdot\mathbf{e}_i)u^i_I - J^{-1}_{1\beta}\sum_{I=1}^{4}\xi^{\beta}_{I}(\mathbf{t}_2\cdot\mathbf{e}_i)u^i_I\right)\\
c_{,\xi^1}|_0 &= \frac{1}{4}\sum_{I=1}^{4}\xi^1_I(\mathbf{t}_3\cdot\boldsymbol{\vartheta}_I) + \frac{1}{8}\left(J^{-1}_{22}\sum_{I=1}^{4}\xi^1_I\xi^2_I(\mathbf{t}_1\cdot\mathbf{e}_i)u^i_I - J^{-1}_{12}\sum_{I=1}^{4}\xi^1_I\xi^2_I(\mathbf{t}_2\cdot\mathbf{e}_i)u^i_I\right) \qquad (127)\\
c_{,\xi^2}|_0 &= \frac{1}{4}\sum_{I=1}^{4}\xi^2_I(\mathbf{t}_3\cdot\boldsymbol{\vartheta}_I) + \frac{1}{8}\left(J^{-1}_{21}\sum_{I=1}^{4}\xi^1_I\xi^2_I(\mathbf{t}_1\cdot\mathbf{e}_i)u^i_I - J^{-1}_{11}\sum_{I=1}^{4}\xi^1_I\xi^2_I(\mathbf{t}_2\cdot\mathbf{e}_i)u^i_I\right)
\end{aligned}$$

5.1.1 Weak Formulation and Linearisation

Since F^P_{RC} is a polynomial of the natural coordinates ξ^1, ξ^2 the integral of Eq. (117) can be determined analytically. That is,

$$\Pi^P_{RC} = \int_{h_-}^{h_+}\int_{\Box} F^P_{RC}\sqrt{a}\; d\xi^1 d\xi^2\; dh = \int_{h_-}^{h_+}\int_{\Box} \bar{c}^2(\xi^1,\xi^2)\sqrt{a}\; d\xi^1 d\xi^2\; dh \approx\; \gamma V\tilde{\Pi}^P_{RC}, \qquad (128)$$

where V is the element volume and

$$\widetilde{\Pi}^P_{RC} = [2c^0 + {}^2\!/_3((c^0_{,\xi^1})^2 + (c^0_{,\xi^2})^2)] \qquad (129)$$

Note that for the following derivations a constant Jacobian is assumed. The force residual vectors and the stiffness matrices in Eq. (121) and Eq. (122) respectively can be determined in a straight forward way. In order to be able to account for warped element geometries a correction has to be introduced. The correction here is introduced like in [16] where the local displacements and rotations are related to their global components via,

$$\begin{bmatrix}\mathbf{u}^l_I\\ \boldsymbol{\vartheta}^l_I\end{bmatrix} = \begin{bmatrix}\mathbf{I} & \widetilde{\mathbf{W}}\\ \mathbf{0} & \mathbf{I}\end{bmatrix}\begin{bmatrix}\mathbf{u}^G_I\\ \boldsymbol{\vartheta}^G_I\end{bmatrix}, \qquad (130)$$

where $\widetilde{\mathbf{W}} = \text{skew}(\mathbf{r}_I)$ is the skew-symmetric matrix is with $\mathbf{r}_I = w_I\mathbf{t}_3$ where w_I is the distance to the middle surface of each node. Analogously forces and moments are transformed as follows,

$$\begin{bmatrix}\mathbf{f}^l_I\\ \mathbf{m}^l_I\end{bmatrix} = \begin{bmatrix}\mathbf{I} & \mathbf{0}\\ \widetilde{\mathbf{W}} & \mathbf{I}\end{bmatrix}\begin{bmatrix}\mathbf{f}^G_I\\ \mathbf{m}^G_I\end{bmatrix} \qquad (131)$$

The warped stiffness matrix of the element is given by,

$$\mathbf{K} = \begin{bmatrix}\mathbf{I} & \mathbf{0}\\ -\widetilde{\mathbf{W}} & \mathbf{I}\end{bmatrix}\mathbf{K}^G\begin{bmatrix}\mathbf{I} & \widetilde{\mathbf{W}}\\ \mathbf{0} & \mathbf{I}\end{bmatrix} \qquad (132)$$

5.2 Numerical Integration of Drill RC Equation

For the case where the area integration is performed numerically, the integrands of Eq. (121) can be determined with the help of Eq. (115) and Eq. (117) in a straight forward way. That is,

$$\frac{\partial F^P_{RC}}{\partial u^i_I} = \gamma c\left[\frac{1}{2}\left(\frac{\partial u_{1,2}}{\partial u^i_I} - \frac{\partial u_{2,1}}{\partial u^i_I}\right)\right], \quad \frac{\partial F^P_{RC}}{\partial \vartheta^i_I} = \gamma\, c\frac{\partial c}{\partial \vartheta^i_I} = \gamma c N_I\, t^i_3 \qquad (133)$$

where the derivatives in Eq. $(133)_1$ read,

$$\frac{\partial u_{1,2}}{\partial u_I^i} = N_{I,2}\,(\mathbf{t}_1 \cdot \mathbf{e}_i), \quad \frac{\partial u_{2,1}}{\partial u_I^i} = N_{I,1}\,(\mathbf{t}_2 \cdot \mathbf{e}_i) \tag{134}$$

The integrands of the force residual vectors and the stiffness matrices in Eq. (121) and Eq. (122) can be determined using a 2-point Gauss quadrature integration scheme. For all the above computations the elemental coordinate system $(\mathbf{t}_i)$ at the element center was used. Although for flat shell elements this is sufficient, for warped geometries the rotation constraint does not account for the element warpage. This problem can be addressed by creating new coordinate systems at every integration point. That is,

$$\mathbf{\Phi}^{h(ip)}_{,\xi^1} = \sum_{I=1}^{4} N^{ip}_{,\xi^1} \mathbf{\Phi}_I, \quad \mathbf{\Phi}^{h(ip)}_{,\xi^2} = \sum_{I=1}^{4} N^{ip}_{I,\xi^2} \mathbf{\Phi}_I, \tag{135}$$

where $\mathbf{\Phi}_I$ is the nodal position vector at the reference shell surface and the superscript ip denotes the integration point. With the above the normal direction is determined as follows,

$$\mathbf{t}_3^{ip} = \frac{\mathbf{\Phi}^{ip}_{,\xi^1} \times \mathbf{\Phi}^{ip}_{,\xi^2}}{\left\|\mathbf{\Phi}^{ip}_{,\xi^1} \times \mathbf{\Phi}^{ip}_{,\xi^2}\right\|} \tag{136}$$

and the plane normal is identified as,

$$\mathbf{t}_1^{ip} = \mathbf{t}_3^{ip} \times \mathbf{t}_2, \quad \mathbf{t}_2^{ip} = \mathbf{t}_3^{ip} \times \mathbf{t}_1^{ip} \tag{137}$$

As such the vectors $\mathbf{t}_i$ should be replaced with the vectors $\mathbf{t}_i^{ip}$ which are determined at every integration point.

6 Numerical Examples

In this section, the performance of the above elements is evaluated based on a set of linear benchmark examples. Besides the quality of the computed displacements, the corresponding stresses and their converge rates are examined. A list of the shell elements that will be considered in the following is given in Table 1. Note that all of the elements below are fully integrated (i.e. 2 point Gauss scheme) quadrilaterals.

Table 1: Elements

Elements	Description
LFS4-RCAI	Linear flat with analytically integrated drill RC, ($\beta = 0.01$).
LFS4-RCFI	Linear flat with numerically integrated drill RC, ($\beta = 0.01$).
LFS4-ERC	Linear flat with numerically integrated enhanced drill RC, ($\beta_t = \beta_w = 0$ and $\beta = 1$).
LFS4-MP	Linear flat based on non-symmetric Biot strain approach, ($\beta = \beta_t = 1$ and $\beta_w = 0.01$).
LFS4+Allman	Linear flat with Allman shape functions
LFS4-MP+Allman	Linear flat based on non-symmetric Biot strain approach with Allman shape functions, ($\beta = \beta_t = 1$ and $\beta_w = 0.01$).
LFS4-RCAI+Allman	Linear flat with analytically integrated drill RC ($\beta = 0.01$) and Allman shape functions
QMHS4	Non-Linear mixed/hybrid with 5/6 Dofs, [18]*
CQUAD4	MSC/NASTRAN
S4	ABAQUS

* Own Results with element of [18].

6.1 Cook's Membrane

This problem was proposed by [11] and it is a very popular benchmark example. It involves a trapezoidal membrane which is clamped on one edge and is subjected to a distributed in-plane bending load on the other, see Figure 1 where the geometrical and material properties are defined.

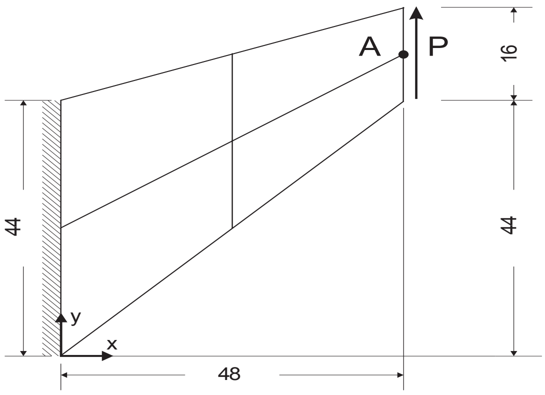

Figure 1: Cook's Membrane: $E = 1$, $\nu = 1/3$, $t = 1$, $P = 1$

In this example, a considerable amount of shear deformation is involved and therefore is excellent for testing the capability of the proposed elements to model membrane dominated situations. Moreover, when quadrilaterals are used for the discretization, the resulting elements are skewed and tapered which makes it even more important since the effects of mesh distortion can also be observed. The results for the vertical displacement and drill rotation at the point A, are listed in Table 2 and Table 3 respectively.

Elements	2×2	4×4	8×8	16×16	32×32
LFS4-RCAI	21.0936	23.0081	23.6850	23.8821	23.9394
LFS4-RCFI	21.1057	23.0135	23.6866	23.8825	23.9395
LFS4-ERC	20.4303	22.7144	23.5491	23.8207	23.9110
LFS4-MP	20.4300	22.7140	23.5486	23.8202	23.9106
LFS4-MP+Allman	22.1472	23.1203	23.6168	23.8296	23.9101
LFS4+Allman	21.2704	23.0663	23.6652	23.8661	23.9312
LFS4-RCAI+Allman	21.1911	23.0361	23.6485	23.8559	23.9260
QMHS4	21.1161	23.0206	23.6891	23.8833	23.9392
S4	20.7115	22.9701	23.6460	23.8588	23.9301
CQUAD4	21.0470	23.0151	23.6881	23.8827	23.9392
Ref.	23.91 [5], 23.936 [39]				

Table 2: Cook's Membrane: Vertical Displacement at point A.

Elements	2×2	4×4	8×8	16×16	32×32
LFS4-RCAI	0.7021	0.7786	0.8431	0.8658	0.8756
LFS4-RCFI	0.7649	0.8254	0.8710	0.8809	0.8838
LFS4-ERC	0.9518	0.7901	0.8464	0.8631	0.8700
LFS4-MP	0.9518	0.7904	0.8502	0.8829	0.8910
LFS4-MP+Allman	0.8662	0.8731	0.8768	0.8860	0.8873
LFS4+Allman	0.8485	0.8906	0.9102	0.9242	0.9268
LFS4-RCAI+Allman	0.8350	0.8842	0.9087	0.9240	0.9197
S4	0.7158	0.7972	0.8504	0.8708	0.8794
CQUAD4	0.7337	0.8102	0.8579	0.8742	0.8805

Table 3: Cook's Membrane: Drill Rotation at Point A.

The sensitivity of the converged solution with respect to the penalty parameter β is shown in Figure 2. The performance of the different methods for the incorporation of the enhancement of strains as described in Section **??** is shown.

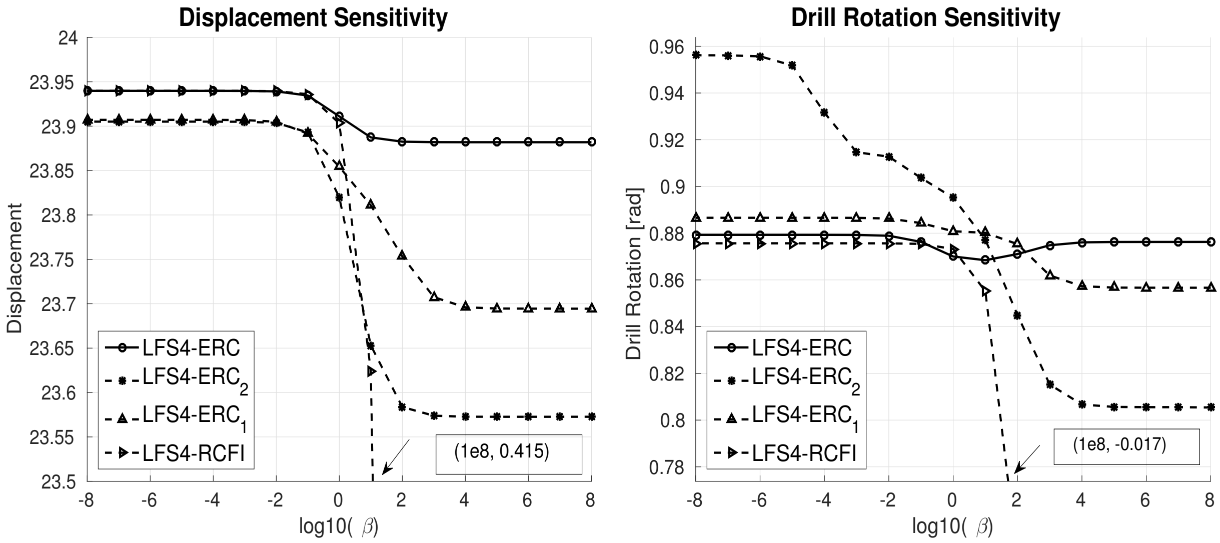

(a) Vertical Displacement (b) Drill Rotation

Figure 2: Cook's Membrane: Sensitivity of computed results with respect to penalty coefficient $\beta = \text{range}(10^8, 10^{-8})$.

It is obvious that the LFS4-ERC implementation, in which the enhanced strains are interpolated according to Eq. (103), has the best performance among all and therefore the implementations LFS4-ERC$_1$, LFS4-ERC$_2$ -using interpolations Eq. (**??**), Eq. (**??**) respectively- will not be considered further. In Figure 3, the effect of the warping parameter β_w is shown.

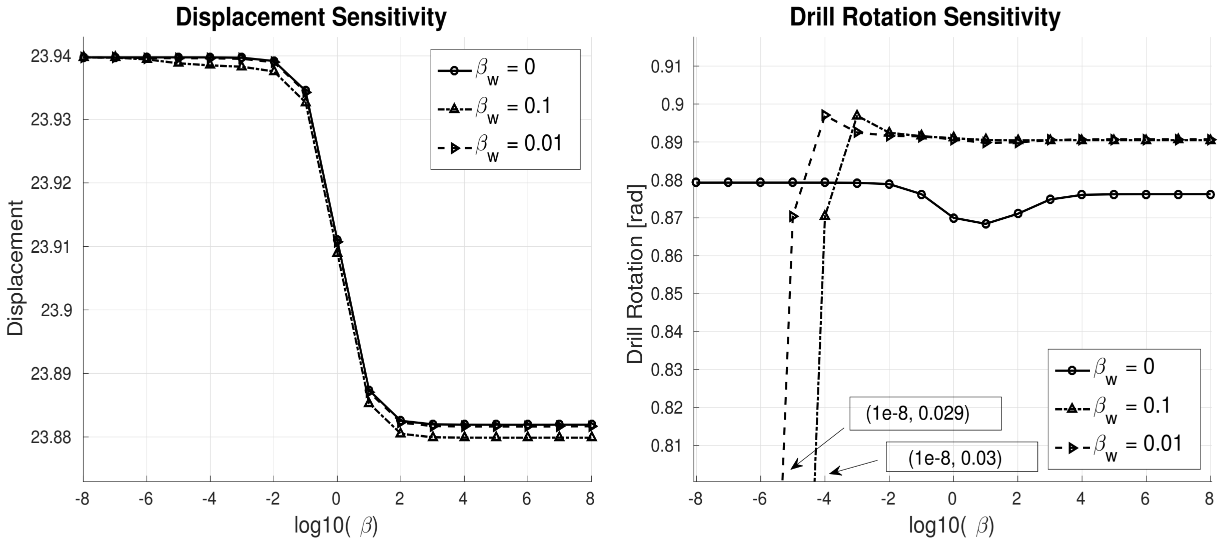

(a) Vertical Displacement (b) Drill Rotation

Figure 3: Cook's Membrane: Sensitivity of LFS4-ERC with respect to penalty parameter β for various warping parameters.

Note that since this is a plane problem the solution shall not depend on the twist parameter β_t which is the case. The convergence of the normal stress resultant $\mathbf{n}^{11}$ for various implementations is plotted in Figure 4. Note that the mesh sizes analysed for the stresses differ from the ones analysed for the displacements. This is due to the fact that stresses are extracted at the centroid[1] and therefore for a meaningful comparison we had to make sure that the centroid of the element from which the stresses are extracted does not change with the mesh refinement. For this example the mesh sizes used are, 6×6, 10×10, 18×18, 34×34, 66×66, 130×130.

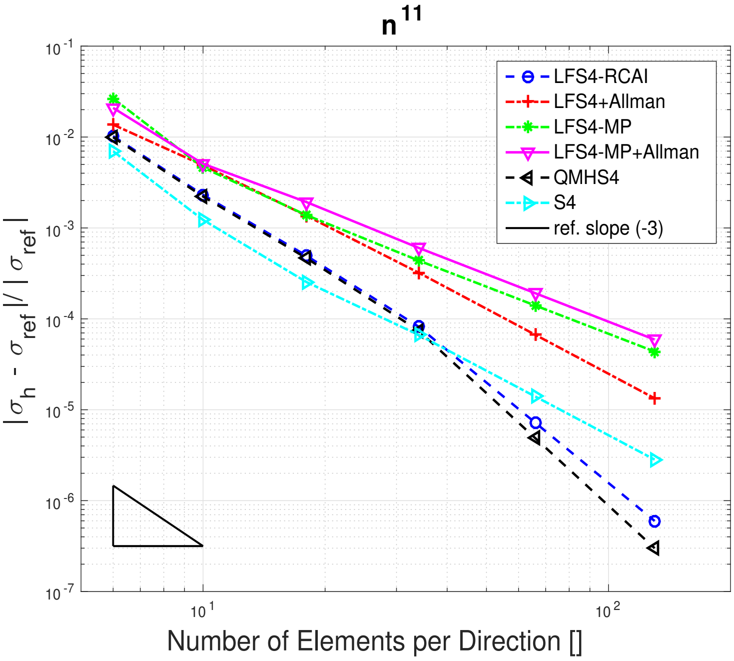

Figure 4: Cook's Membrane: Rate of convergence of stress resultant

The reference value, σ_{ref}, for the error estimation is obtained using Richardson's extrapolation, see [7] and also [8] where a remedy for oscillatory converge is presented. The extrapolated value is computed using the stresses as computed from the last three finer meshes.

6.2 Cantilever Under end Moment

This example involves a straight cantilever beam which is subjected to an in-plane end moment at one end while the other is fully clamped.

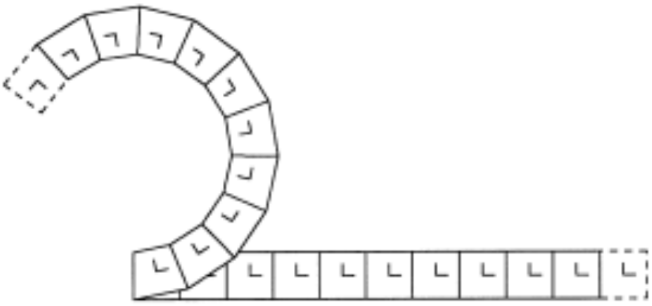

Figure 5: Cantilever under end moment: $E = 1200$, $l = 10$, $h = t = 1$, $\nu = 0.3$, $M = 0.1$

---

[1] Although the stresses are computed at the integrations points, here it was decided to make the stress comparison based on the centroidal values. For the case of four node quadrilaterals, it can be proved that the centroid is the Barlow point and therefore it is expected to have the highest convergence rate.

This is a very important example since the ability of the proposed element to carry drill moments can be tested. In Table 4, the vertical displacement and drill rotation of the tip of the cantilever are listed.

	10×1	
Elements	Vertical	Rotation
LFS4-RCAI	0.0457	0.0097
LFS4-RCFI	0.0457	0.0097
LFS4-ERC	0.0501	0.0103
LFS4-MP	0.0497	0.0103
LFS4-MP+Allman	0.0497	0.0103
LFS4+Allman	0.0455	0.0351
S4	0.0467	0.0121
Analytical	0.05	0.01

Table 4: Cantilever under tip moment: Vertical displacement and drill rotation at the tip of the beam.

Note that in the above the results corresponding to LFS4-RCAI, LFS4-RCFI implementations are obtained with a penalty parameter $\beta = 1$. As it is already reported in the literature, examples where drill moments are involved require a larger penalty parameter. The main advantage of the proposed implementation LFS4-ERC is that higher penalty parameters can be used without affecting the element performance in other examples. To illustrate this, the sensitivity of the computed values with respect to the penalty parameter is shown in Figure 6.

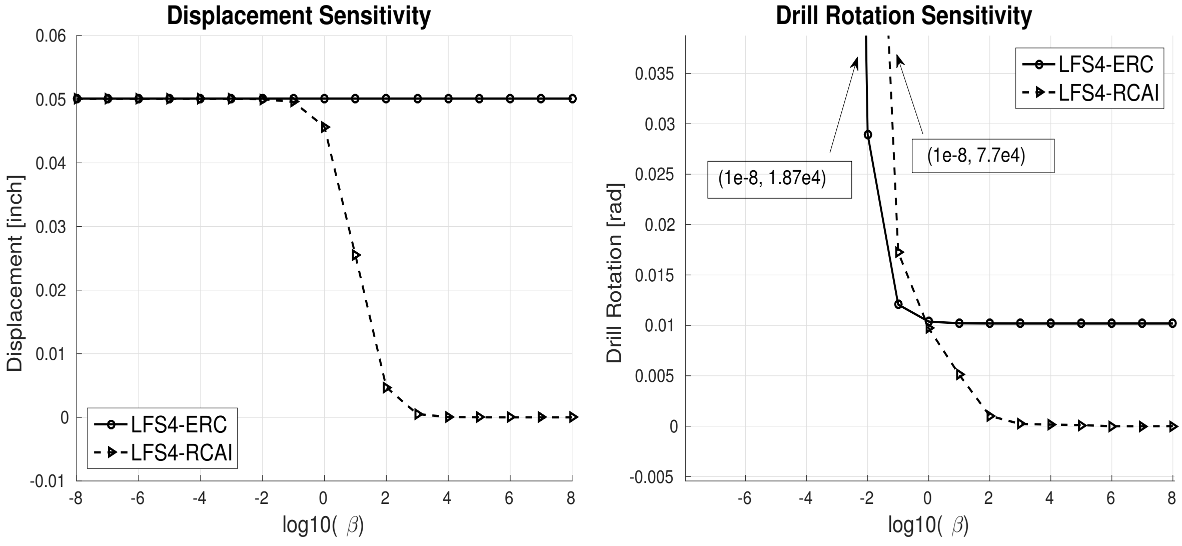

(a) Tip Displacement (b) Tip Drill Rotation

Figure 6: Cantilever under tip moment: Sensitivity of computed results with respect to penalty coefficient $\beta = \mathrm{range}(10^8, 10^{-8})$

Clearly, the performance of the proposed element is superior to LFS4-RCAI which for larger penalty parameters becomes unacceptably stiff. Of course for small penalty parameters the drill rotation for both formulations is unbounded. The effect of the warping parameter β_w on the computed solutions for the LFS4-ERC is shown in Figure 7.

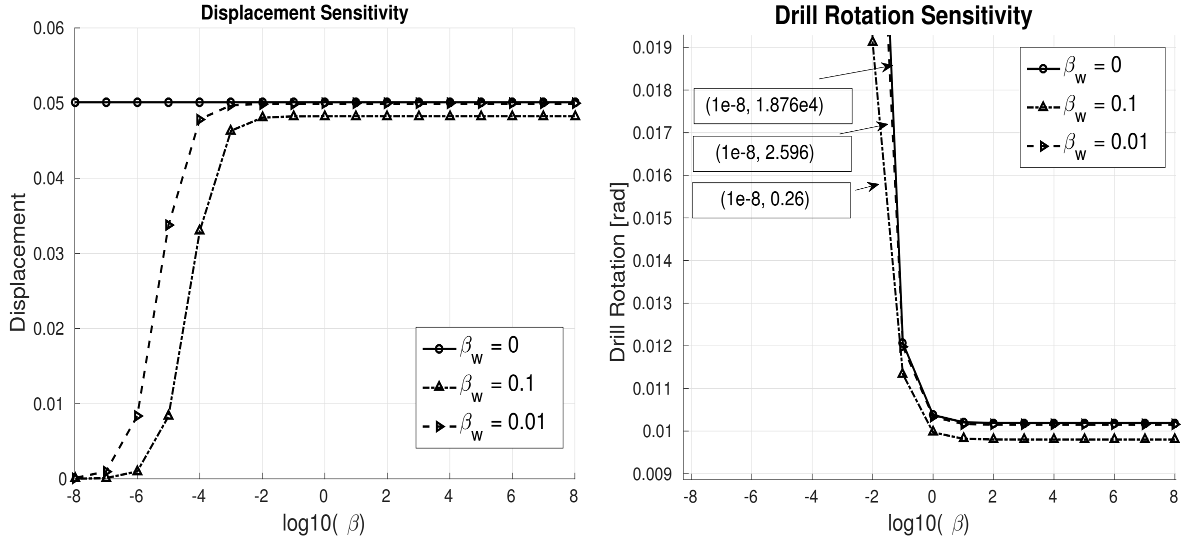

(a) Tip Displacement (b) Tip Drill Rotation

Figure 7: Cantilever under tip moment: Sensitivity of LFS4-ERC with respect to penalty parameter β and warping parameter β_w.

6.3 Pinched Hemispherical Shell

The third example involves a hemispherical shell, subjected to two inward and outward point loads $90°$ apart. Due to the double symmetry, only one quadrant can be modelled and symmetry boundary conditions can be applied. This example is popular for multiple reasons, firstly it involves a double curvature structure and secondly the shell undergoes an almost inextensional bending deformation.

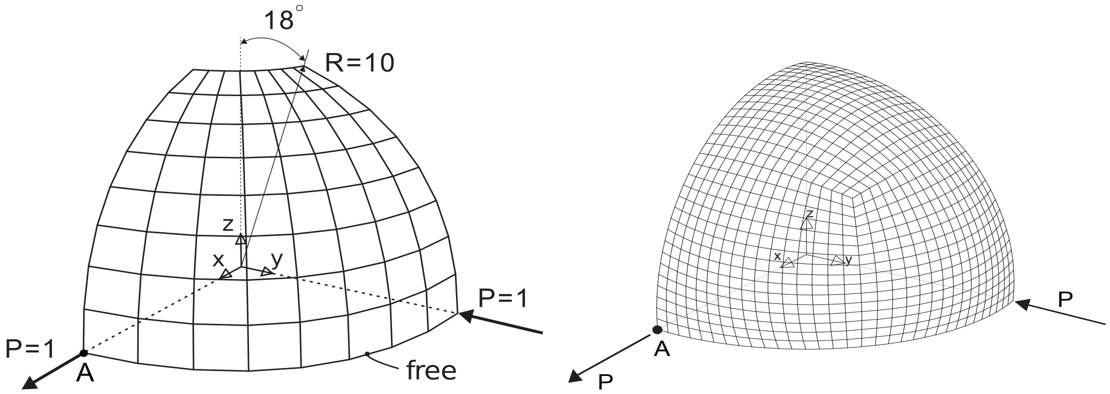

(a) Pinched Hemispherical Shell with hole (b) Pinched Hemispherical Shell without hole

Figure 8: Pinched Hemispherical Shells. $E = 6.825 \times 10^7$, $\nu = 0.3$, $h = 0.04$, $P = 1$

Two variants of this test exist in the literature. The first was proposed by [23] where a hole of $18°$ is introduced at the top in order to avoid the use of triangles near the axis of revolution, see Figure 8. In this case, the resulted finite elements are planar and therefore the effect of warp is not present. The computed displacements for the point A are listed in Table 5. Note that the displacement of both loaded points should be identical for the case of linear static analysis due to symmetry.

Elements	4×4	8×8	16×16	32×32
LFS4-RCAI	9.0662	9.2295	9.2943	9.3351
LFS4-RCFI	8.6881	9.2457	9.3067	9.3387
LFS4-ERC	9.1400	9.3010	9.3137	9.3401
LFS4-MP	9.0603	9.2714	9.3043	9.3373
LFS4-MP+Allman	3.7017	8.9415	9.3086	9.3431
LFS4+Allman	3.4786	8.9246	9.3078	9.3427
LFS4-RCAI+Allman	3.4361	8.8675	9.2927	9.3388
QMHS4	9.6631	9.3781	9.3333	9.3454
S4	9.1966	9.2562	9.2997	9.3364
CQUAD4	9.5071	9.4478	9.3661	9.3574
Ref.	9.4 [23], 9.3 [33]			

Table 5: Pinched Hemispherical Shell with Hole: Displacement $-u_1 \times 100$

In Figure 9a, the sensitivity with respect to the penalty parameter β is plotted. Mooreover, in Figure 9b, the effect of the warping parameter for the LFS4-ERC implementation is shown.

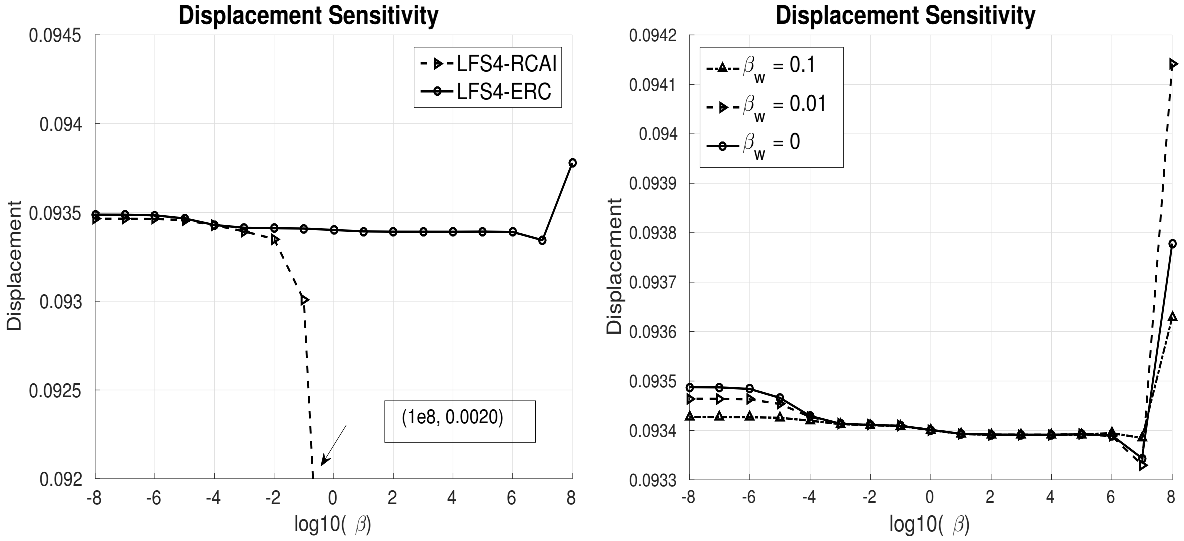

(a) Comparison with LFS4-RCAI

(b) Effect of warping parameter on LFS4-ERC

Figure 9: Pinched Hemispherical Shell with Hole: Sensitivity of computed results with respect to penalty coefficient $\beta = \mathrm{range}(10^8, 10^{-8})$ and warping parameter β_w.

The advantage of the enhanced drill rotation constraint is apparent since even for doubly curved problems the computed solutions are almost insensitive to the penalty parameter. Unlike the previous examples, being all plane, here it is instructive to study the effect of the twist parameter β_t for the LFS4-ERC element. In Figure 10 the sensitivity of the computed displacement is plotted.

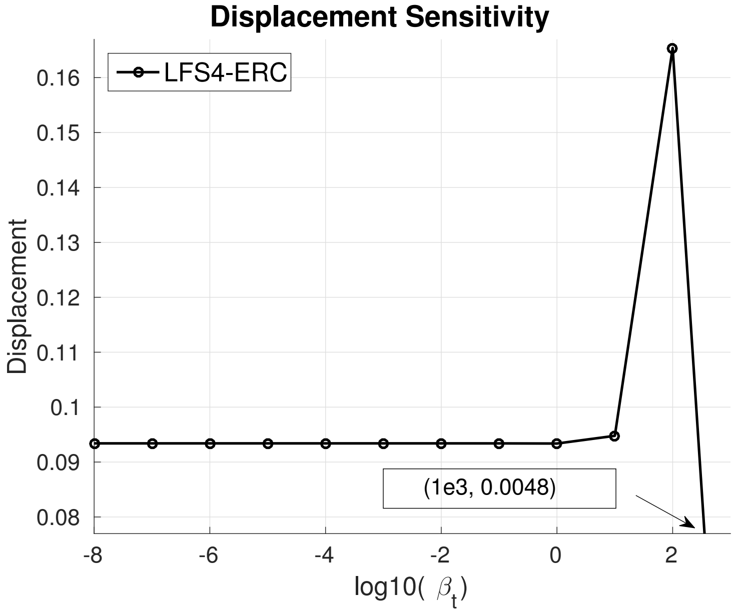

Figure 10: Pinched Hemispherical Shell with Hole: Sensitivity of LFS4-ERC with respect to the twist parameter, $\beta_t = \mathrm{range}(10^3, 10^{-8})$.

The above figure clearly dictates that the incorporation of the twist parameter impairs the solution while for $\beta_t < 1$ the result almost remains constant. The selection of $\beta_t = 0$ can be justified. The second variant of the pinched hemispherical problem, see Figure 8b does not involve a hole but the resulted elements are highly skewed and warped especially for coarse discretizations. The computed displacements for this case are listed in Table 6.

Elements	4×4	8×8	16×16	32×32
LFS4-RCAI	8.3951	8.9468	9.1254	9.2049
LFS4-RCFI	7.8903	9.0457	9.1698	9.2177
LFS4-ERC	8.7632	9.1741	9.1889	9.2219
LFS4-MP	8.6820	9.1428	9.1789	9.2188
LFS4-MP+Allman	3.0762	8.6649	9.1755	9.2270
LFS4+Allman	2.8801	8.6630	9.1749	9.2261
LFS4-RCAI+Allman	2.7853	8.4383	9.1101	9.2095
QMHS4	5.2690	9.0300	9.1983	9.2264
S4	4.7672	8.8644	9.1628	9.2193
CQUAD4	9.0688	9.3113	9.2479	9.2425
Ref.		9.24 [33]		

Table 6: Pinched Hemispherical Shell without hole: Displacement $-u_1 \times 100$

Closing this example, the convergence of the torsional moment for the hemispherical shell with the hole is shown in Figure 11. For this example the mesh sizes used are, 10×10, 18×18, 34×34, 66×66 and correspond to the one quadrant of the hemisphere.

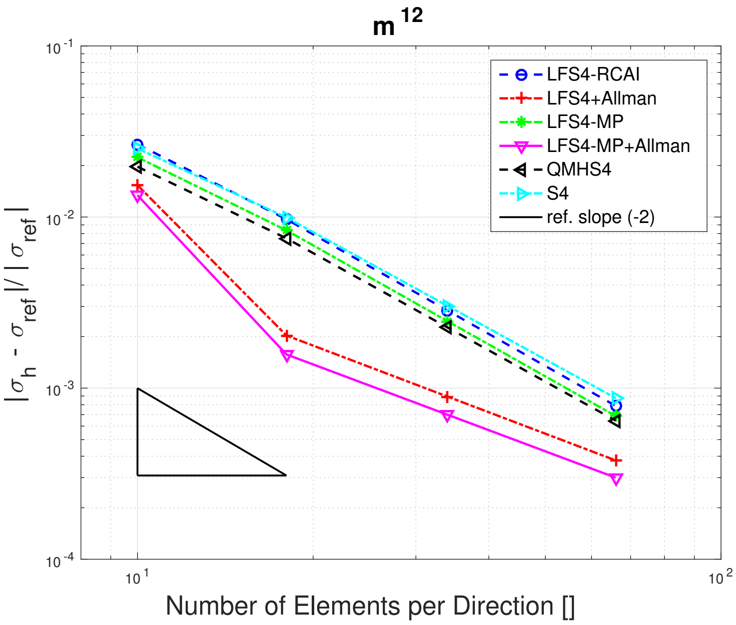

Figure 11: Pinched Hemispherical Shell with Hole: Rate of convergence of resultant torsional moment.

6.4 Raasch Hook

The Raasch hook or Raasch challenge as it is usually referred to involves a thick curved strip - essentially a hook like geometry - which is clamped on one edge and is subjected to a distributed unit tip in-plane shear load on the other, see Figure 12. The hook is composed out of two cylindrical segments of radius R_1, R_2 which span an opening angle of $60°$and $150°$respectively. The geometric as well as the material properties are shown in Figure 12. This example was first reported by I. Raasch of BMW in 1990 and revealed an erroneous behaviour (i.e. solution failed to converge with the mesh refinement) of the QUAD4 element of the MSC/NASTRAN FE code.

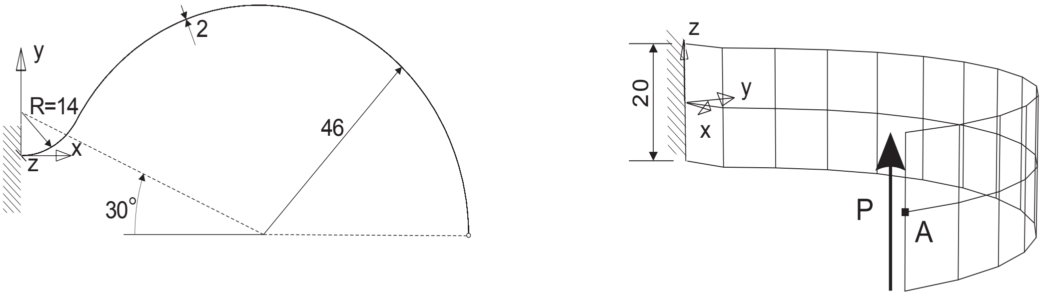

Figure 12: Raasch's Hook: Initial geometry, $E = 3300,\ \nu = 0.35,\ h = 2,\ P = 1$

In [24], it was found that the problem was caused by the treatment of the shell normals and resulted in an inability to transfer correctly the twisting moments. This failure introduced significant transverse shears whose effect was greater with the mesh refinement since the drill rotation was less and less restrained by the bending stiffness of an adjacent element. In Table 7 and Table 8 the displacements and drill rotations at the point A of the loaded edge are listed

Elements	9×1	18×3	36×5	72×10	144×20
LFS4-RCAI	4.4376	4.6786	4.7987	4.9103	4.9769
LFS4-RCFI	4.4376	4.6786	4.7987	4.9103	4.9769
LFS4-ERC	4.4297	4.6085	4.6904	4.7761	4.8310
LFS4-MP	4.3799	4.5912	4.6731	4.7316	4.7581
LFS4-MP+Allman	4.3799	4.5890	4.6712	4.7313	4.7580
LFS4+Allman	4.4136	4.6917	5.0562	6.2416	10.528
LFS4-RCAI+Allman	4.4048	4.6293	4.7397	4.8599	4.9458
QMHS4	4.5462	4.6668	4.7109	4.7850	4.8368
S4	4.8531	4.8799	4.9541	5.0107	5.0335
CQUAD4	4.592	4.7105	4.7308	4.7252	4.7194
Ref.	4.9352 [19]				

Table 7: Raasch Hook: Vertical Displacement at Point A.

Elements	9×1	18×3	36×5	72×10	144×20
LFS4-RCAI	0.0235	0.0251	0.0259	0.0266	0.0270
LFS4-RCFI	0.0235	0.0251	0.0259	0.0266	0.0270
LFS4-ERC	0.0236	0.0247	0.0252	0.0256	0.0260
LFS4-MP	0.0231	0.0246	0.0251	0.0254	0.0256
LFS4-MP+Allman	0.0231	0.0246	0.0251	0.0254	0.0255
LFS4+Allman	0.0230	0.0240	0.0227	0.0161	-0.0110
LFS4-RCAI+Allman	0.0231	0.0246	0.0254	0.0261	0.0267
QMHS4	0.0134	0.0198	0.0227	0.0244	0.0253
S4	0.0257	0.0261	0.0265	0.0268	0.0269
CQUAD4	0.0247	0.0252	0.0253	0.0253	0.0253

Table 8: Raasch Hook: Drill Rotation at Point A.

In Figure 13, the sensitivity of the converged solutions with respect to the penalty parameter is plotted.

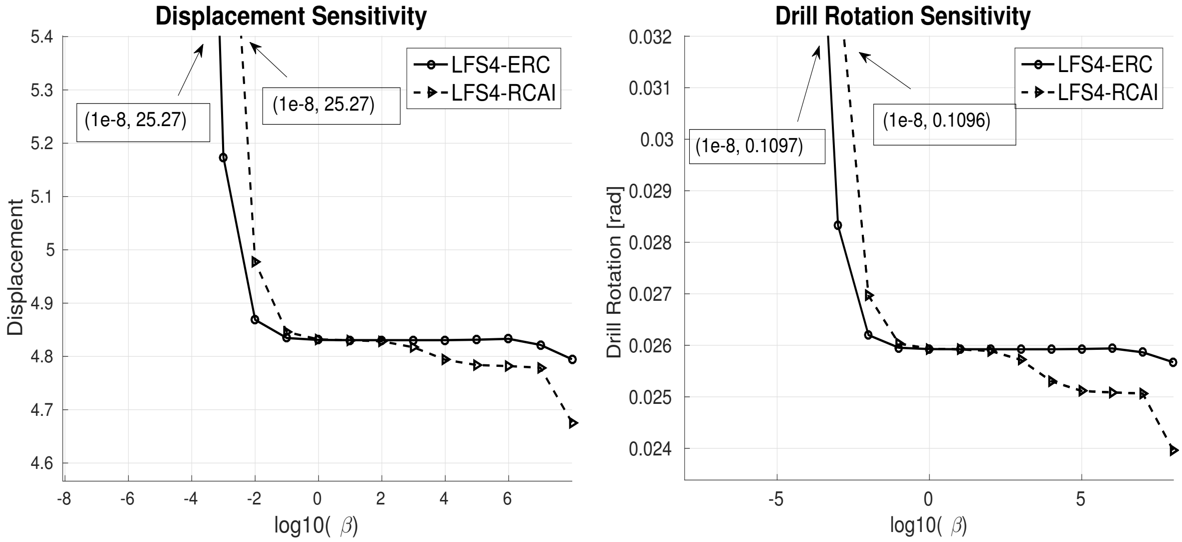

(a) Vertical Displacement (b) Drill Rotation

Figure 13: Raasch Hook: Sensitivity of computed results with respect to penalty coefficient $\beta = \mathrm{range}(10^8, 10^{-8})$.

Again the sensitivity of the computed results with respect to the twist parameter β_t is illustrated in Figure 14

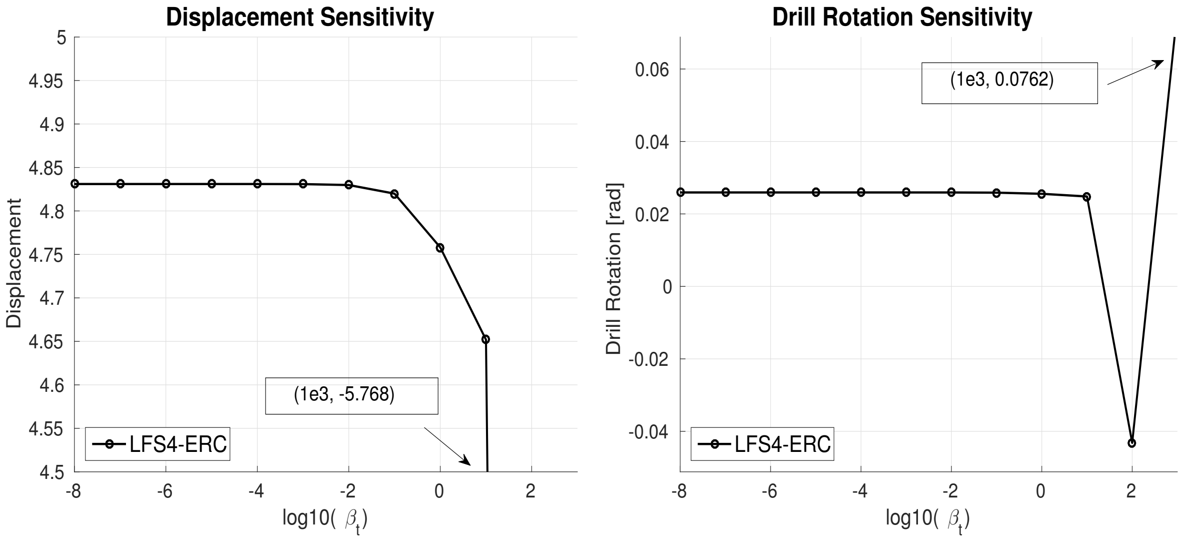

(a) Vertical Displacement

(b) Drill Rotation

Figure 14: Raasch Hook: Sensitivity of LFS4-ERC with respect to the twist parameter $\beta_t = \mathrm{range}(10^3, 10^{-8})$.

In Figure 15, the convergence of the stress resultant torsional moment is shown. For the Raasch Hook the mesh sizes analysed for the stress comparison are, 46×6, 82×10, 138×18 and 248×34.

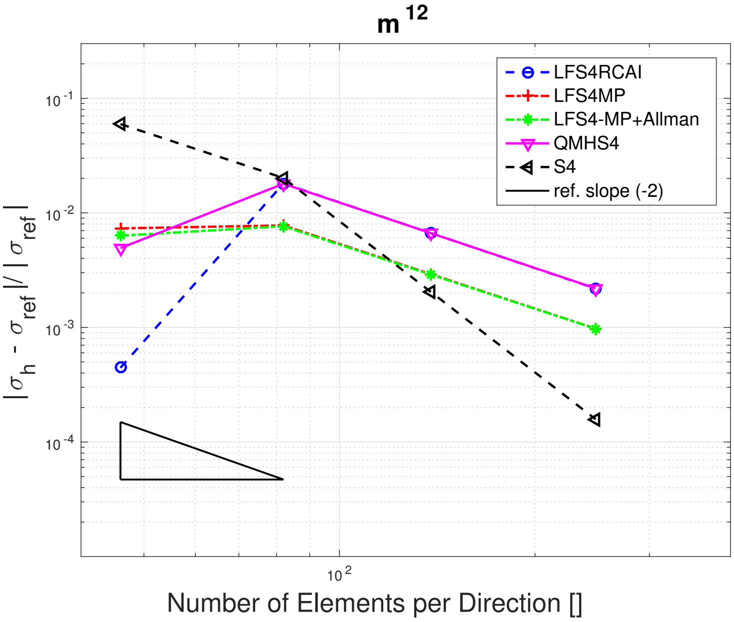

Figure 15: Raasch Hook: Rate of convergence of resultant torsional moment.

6.5 Pre-Twisted Beam

This test was initially proposed by [23] and it is very valuable since the effect of element warpage can be assessed. Although each element is approximately $7.5°$ warped, this amount can have quite significant effects, see [4]. The initial geometry of the beam is twisted by $90°$ with this being a stress free configuration. One edge is clamped while the other is subjected separately to three different concentrated loads at the tip. Thus the three load-cases are i) a unit shear load in width direction and ii) a unit shear load in thickness direction and iii) a unit axial load. Note that for the latter the initial twost of the beam is $180°$. The material as well as geometrical properties are given in Figure 16.

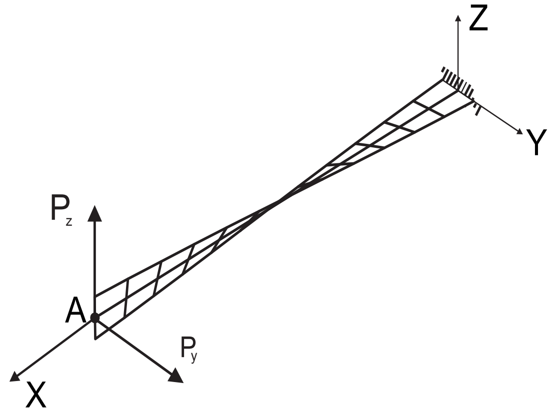

Figure 16: Pre-Twisted Beam Configuration: $E = 2.9 \times 10^7$, $\nu = 0.22$, $L = 12$, $w = 1.1$, twist=90°, $P_y = P_z = 1 \times 10^{-6}$ and thickness $h = 0.0032$

In [23], the thickness is $h = 0.32$ however, in [4] a thinner variant (i.e. $h = 0.0032$) is used in order to invoke membrane locking phenomena that are more significant for thinner shells. In the latter, the significance of accounting for the variation of the Jacobian through the thickness, i.e. account for curvature-displacement coupling, is illustrated. In the absence of these terms, an error as large as 70% can occur. The following results correspond to the thin case and the reference solutions are based on beam theory. The computed displacements for all loadcases are listed in Table 9, Table 10 and Table 11.

Elements	2×12	4×24	8×48
LFS4-RCAI	5.2781	5.2264	5.2421
LFS4-RCFI	5.2027	5.2358	5.2462
LFS4-ERC	5.2801	5.2374	5.2463
LFS4-MP	5.2757	5.2370	5.2460
LFS4-MP+Allman	5.2064	5.2351	5.2463
QMHS4	5.1768	5.2310	5.2462
S4	5.1969	5.2377	5.2482
CQUAD4	5.2674	5.2427	5.2471
Ref.		5.256 [4]	

Table 9: Pre-Twisted Beam: Load Case 1, In plane Displacement $100 \times u_2$

Elements	2×12	4×24	8×48
LFS4-RCAI	1.2990	1.2918	1.2925
LFS4-RCFI	1.2955	1.2932	1.2930
LFS4-ERC	1.2990	1.2936	1.2931
LFS4-MP	1.2989	1.2936	1.2931
LFS4-MP+Allman	1.2954	1.2933	1.2931
QMHS4	1.2691	1.2874	1.2917
S4	1.2748	1.2894	1.2922
CQUAD4	1.2791	1.2888	1.2919
Ref	1.294 [4]		

Table 10: Pre-Twisted Beam: Load Case 2, Out of plane Displacement $100 \times u_3$

Elements	2×12	4×24	8×48
LFS4-RCAI	6.197	4.482	4.479
LFS4-RCFI	4.885	4.812	4.493
LFS4-ERC	8.465	4.848	4.571
LFS4-MP	8.503	4.842	4.570
QMHS4	4.725	4.512	4.404
S4	3.445	4.153	4.290

Table 11: Pre-Twisted Beam: Load Case 3, Axial Displacement $10^5 \times u_3$

For the last load case the results of the LFS4-MP+Allman element are bad and therefore not included. In Figure 17, the sensitivity of the displacement with respect to the penalty parameter β for the first two load cases is plotted.

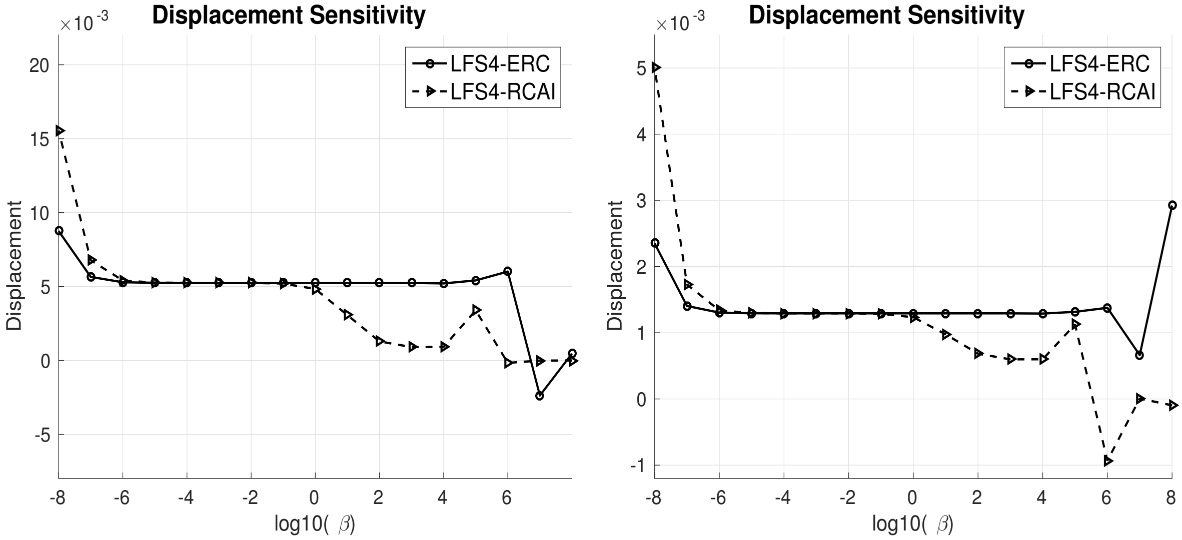

(a) Load Case 1

(b) Load Case 2

Figure 17: Pre-Twisted Beam: Sensitivity of computed results with respect to penalty parameter $\beta = \text{range}(10^8, 10^{-8})$.

In Figure 18, the sensitivity with respect to the twist parameter for the LFS4-ERC is plotted. Note that only the first two load case are considered.

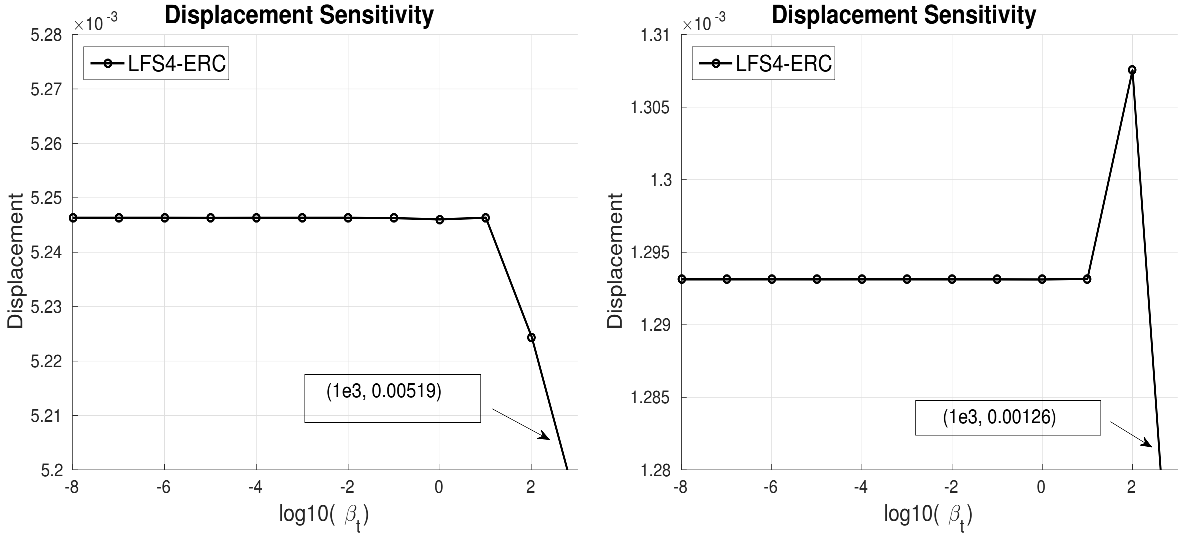

(a) Load Case 1

(b) Load Case 2

Figure 18: Pre-Twisted Beam: Sensitivity of LFS4-ERC with respect to the twist parameter $\beta_t = \text{range}(10^3, 10^{-8})$.

Again the selection of a zero twist penalty parameter can be justified. Closing this example the convergence of the membrane stress resultant SF1 is shown for both load cases in Figure 19a and Figure 19b. For this examples the mesh sizes used are, 10×2, 34×6, 66×10, 130×18.

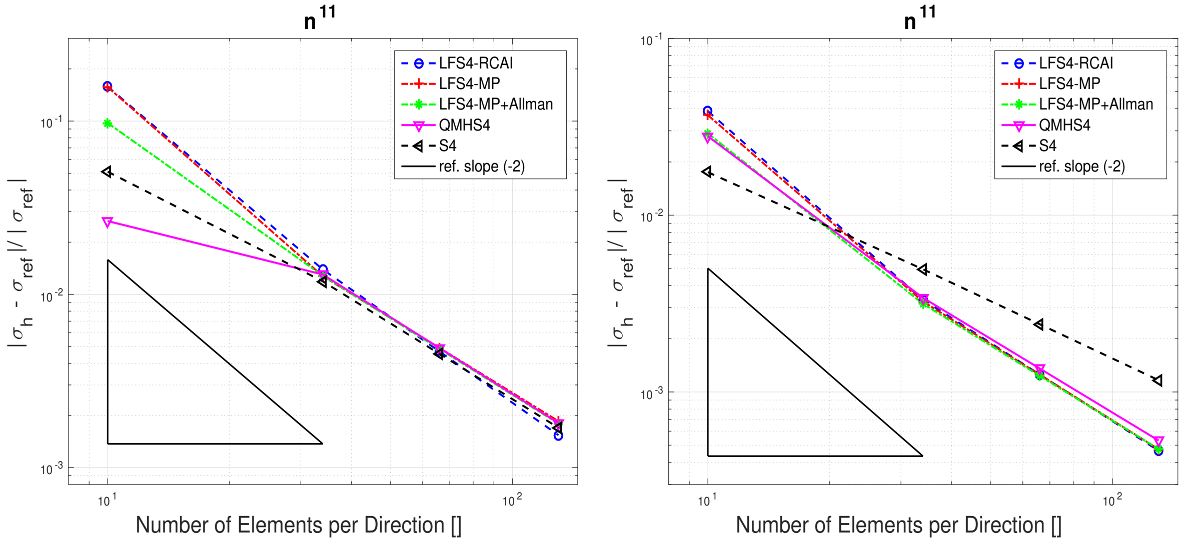

(a) Load Case 1

(b) Load Case 2

Figure 19: Pre-Twisted Beam: Rate of convergence of resultant axial force for out-of plane shear load.

6.6 Pinched Cylinder with End Diaphragm

The fifth example involves a cylindrical shell with rigid diaphragms at both ends and is subjected to two opposing forces which are applied at the middle. The geometrical as well as the material characteristics are shown in Figure 20. Here it is important to note that in the literature exist alternative geometrical and material properties, compare [27] and [33]. Here the latter is used. This is a very popular test since it involves inextensional bending deformation, finite rotations and quite complex stress states. Firstly, it was used by [22] and later by [3] for testing their MITC elements.

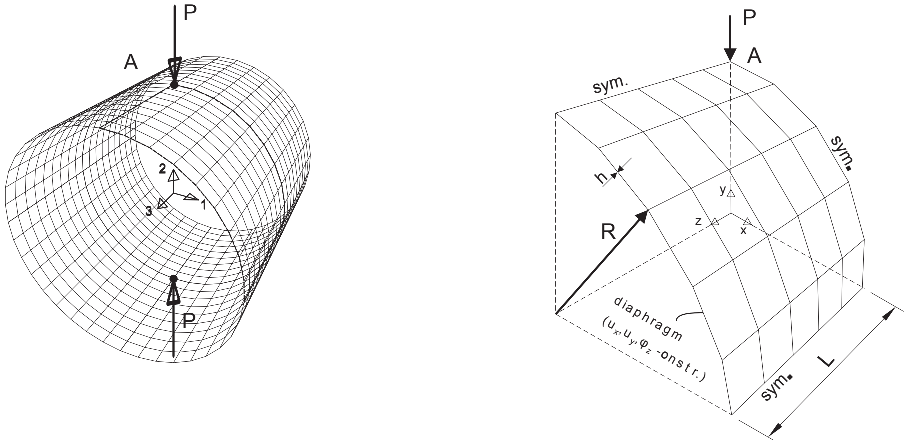

Figure 20: Pinched Cylinder with end diaphragms. Initial Geometry, $E = 3 \times 10^6$, $R = 300$, $L = 300$, $\nu = 0.3$, $h = 3$.

Taking advantage of the symmetry, only one-eighth of the cylinder is modelled. The vertical displacements of point A for a linear static analysis are listed in Table 12.

Elements	10×10	20×20	40×40
LFS4-RCAI	1.517	1.749	1.820
LFS4-RCE7	1.517	1.749	1.820
LFS4-ERC	1.508	1.749	1.820
LFS4-MP	1.497	1.742	1.818
LFS4-MP+Allman	1.488	1.740	1.817
QMHS4	1.532	1.758	-
S4	1.519	1.750	1.821
Ref.	1.8249 [33]		

Table 12: Pinched with end diaphragms: Vertical Displacement at Point A, $-u_3 \times 10^5$

The sensitivity of the computed displacement with respect to the penalty parameter and also the effect of the warping penalty parameter β_w for the LFS4-ERC implementation are shown in Figure 21.

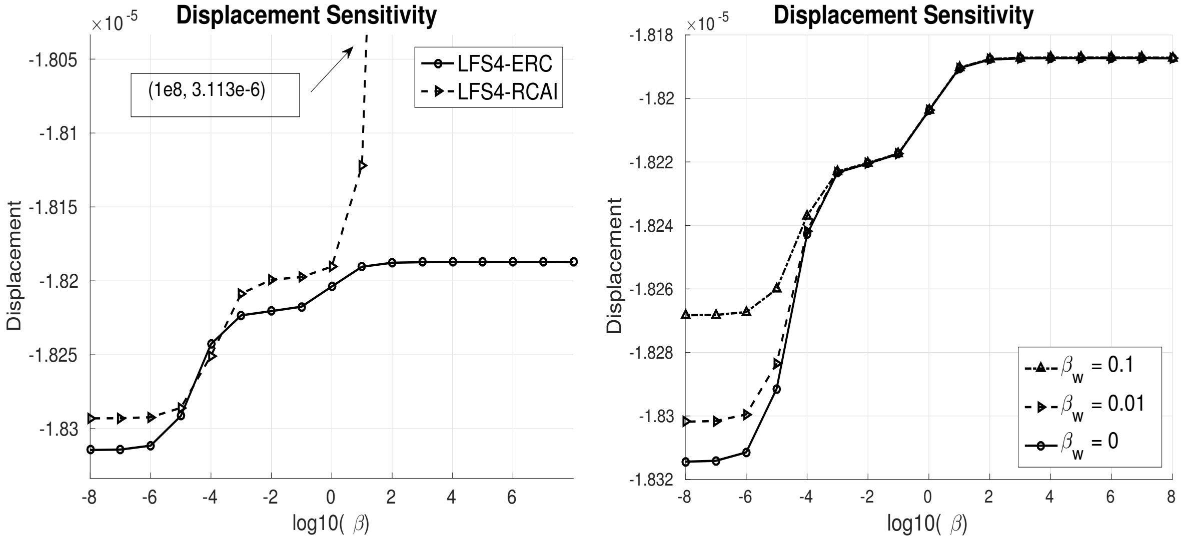

(a) Comparison with LFS4-RCAI (b) Effect of warping parameter on LFS4-ERC

Figure 21: Pinched Cylinder with end diaphragms: Sensitivity of computed results with respect to penalty coefficient $\beta = \mathrm{range}(10^8, 10^{-8})$.

The sensitivity with respect to the twist parameter for the LFS4-ERC is plotted in Figure 22.

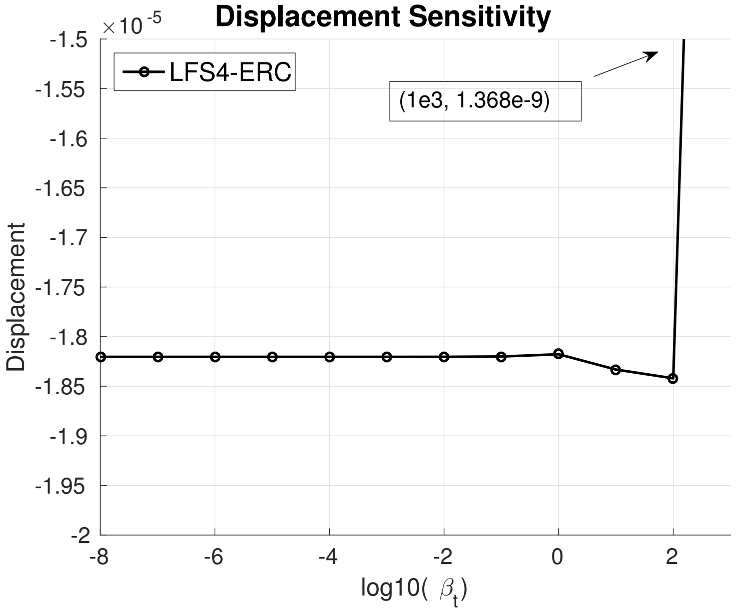

Figure 22: Pinched Cylinder with end diaphragms: Sensitivity of LFS4-ERC with respect to the twist parameter $\beta_t = \mathrm{range}(10^3, 10^{-8})$.

Closing, the convergence of the resultant bending moment is shown in Figure 23. For this example the mesh sizes used are, 10×10, 18×18, 34×34, 66×66.

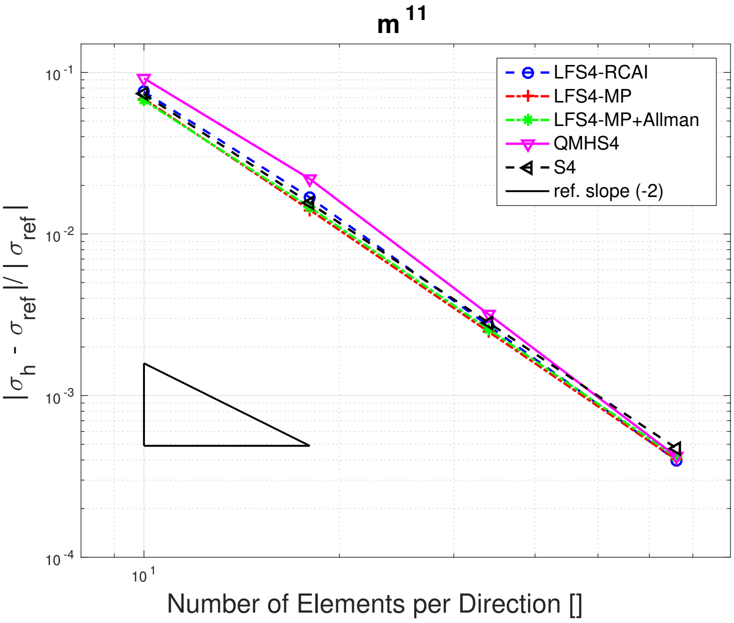

Figure 23: Pinched Cylinder with end Diaphragms: Rate of convergence of resultant bending moment.

6.7 C- Channel Section

The last benchmark example involves a short C-beam which is fully clamped at one end and is loaded by a vertical force at the other. The direction of the applied load is parallel to the web of the C-Section. The geometric as well as material properties are given in Figure 24. This test was proposed in [9] and it is a benchmark test where a drilling degree of freedom is required. This is due to the fact that at the juncture the rotations associated with flexure will induce in-plane twisting in the adjacent elements.

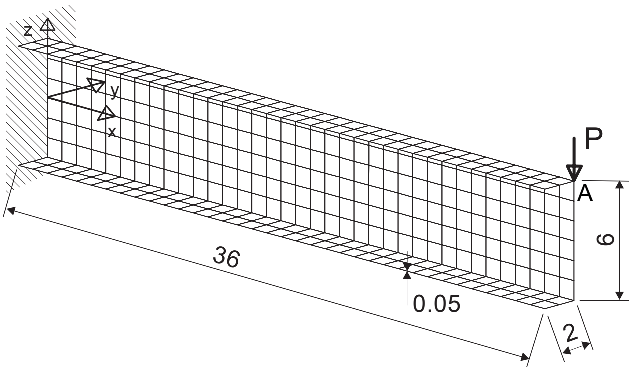

Figure 24: C-Section Channel Beam. $E = 10^7,\ \nu = 0.333,\ h = 0.05,\ P = 1$

The computed displacements as well as the drill rotation of point A are listed in Table 13 and Table 14 respectively.

Elements	18×5	36×10	72×20	144×40	288×80
LFS4-RCAI	1.1492	1.1540	1.1576	1.1604	1.1628
LFS4-RCFI	1.1491	1.1540	1.1576	1.1604	1.1628
LFS4-ERC	1.1477	1.1530	1.1569	1.1599	1.1624
LFS4-MP	1.1476	1.1530	1.1569	1.1599	1.1624
LFS4-MP+Allman	1.1493	1.1544	1.1585	1.1616	1.1638
LFS4+Allman	1.1118	1.1451	1.1565	1.1613	1.1639
QMHS4	1.1496	1.1542	1.1577	1.1605	1.1628
S4	1.1488	1.1538	1.1575	1.1603	1.1627
CQUAD4	1.1450	1.1544	1.1578	1.1605	1.1626

Table 13: C-Section Channel Beam: Vertical Displacement $-u_1 \times 1000$

Elements	18×5	36×10	72×20	144×40	288×80
LFS4-RCAI	1.0178	1.0359	1.0585	1.0953	1.1508
LFS4-RCE7	1.0210	1.0348	1.0578	1.0951	1.1508
LFS4-ERC	1.0133	1.0333	1.0650	1.0951	1.1508
LFS4-MP	1.0139	1.0343	1.0650	1.1134	1.1872
LFS4-MP+Allman	1.0491	1.0874	1.1624	1.2912	1.4432
LFS4+Allman	0.9831	1.0684	1.1552	1.2814	1.4135
QMHS4	1.0270	1.0366	1.0586	1.0955	1.1513
S4	1.0239	1.0354	1.0577	1.0970	1.1617
CQUAD4	1.0227	1.0373	1.0565	1.0904	1.1423

Table 14: C-Section Channel Beam: Drill Rotation $u_6 \times 10^4$

The meshes used correspond to $n \times m$ elements where n is the number of elements in length direction and m is the total number of elements through the width and height. The sensitivity of the computed results with respect to the penalty parameter β is shown in Figure 25.

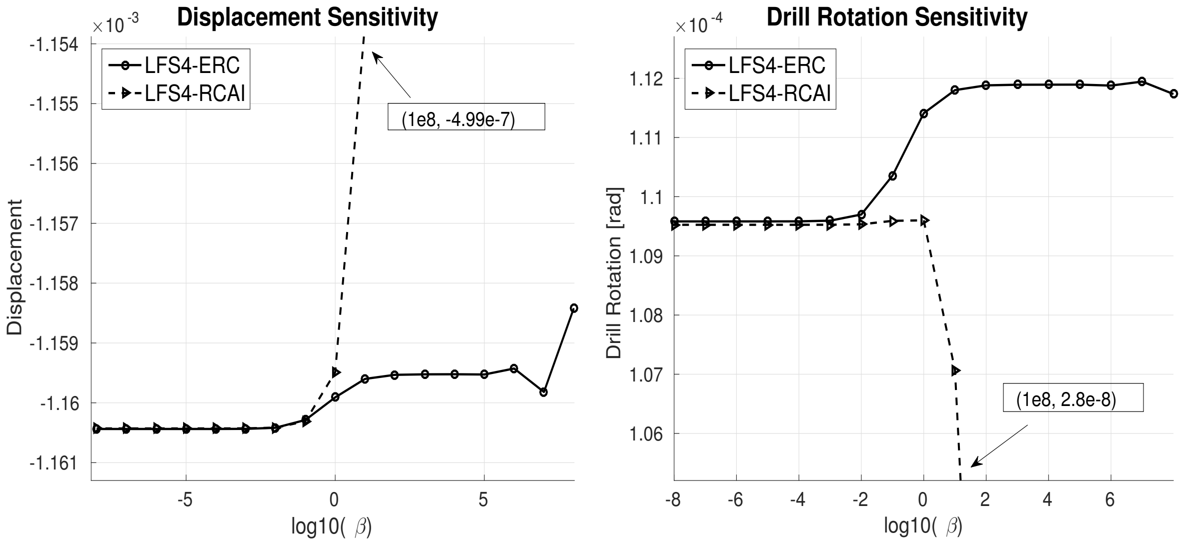

(a) Vertical Displacement

(b) Drill Rotation

Figure 25: C-Section: Sensitivity of computed results with respect to penalty parameter $\beta = \mathrm{range}(10^8, 10^{-8})$.

In Figure 26, the behaviour of the LFS4-ERC for various warping parameters is shown.

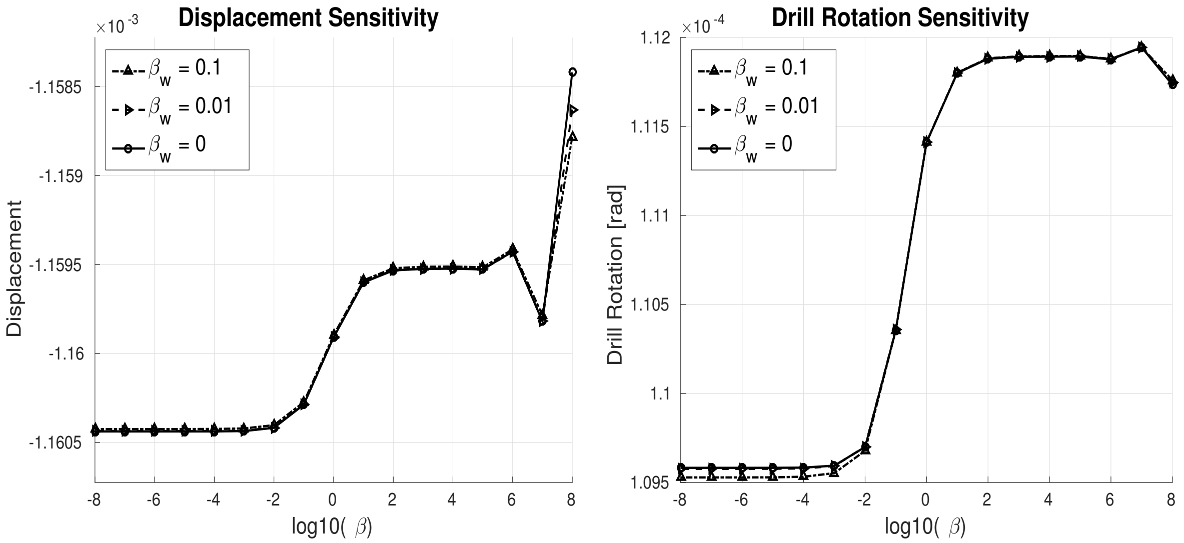

(a) Vertical Displacement (b) Drill Rotation

Figure 26: C-Section: Sensitivity of LFS4-ERC with respect to penalty parameter β for various warping parameters.

Lastly, the sensitivity of the computed solutions with respect to the twist parameter is plotted in Figure 27.

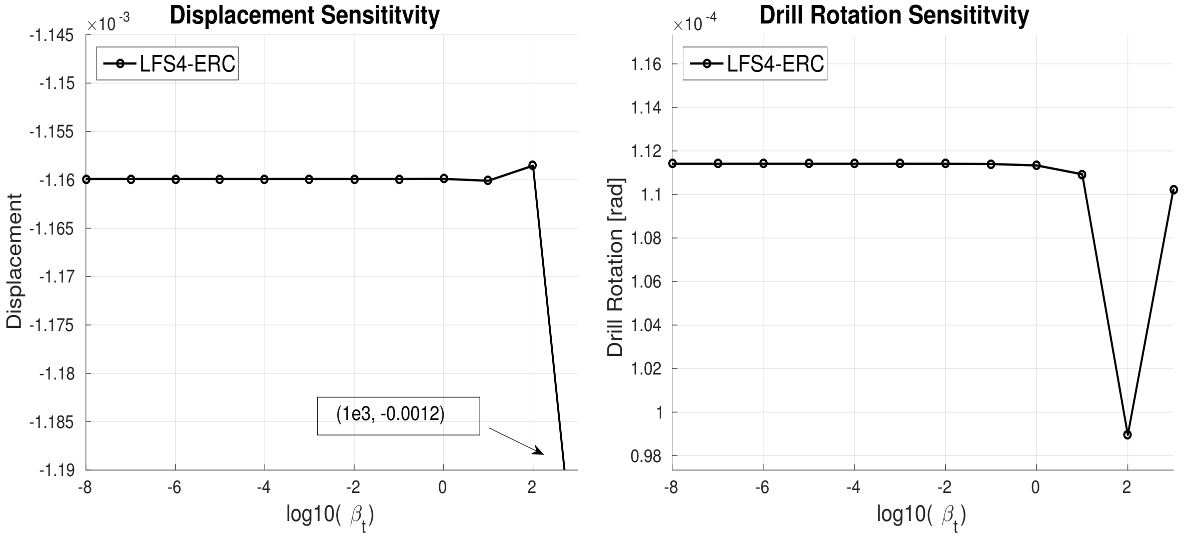

(a) Vertical Displacement (b) Drill Rotation

Figure 27: C-Section: Sensitivity of displacement with respect to the twist coefficient $\beta_t = \mathrm{range}(10^3, 10^{-8})$.

7 Conclusions

It has been demonstrated that by introducing a proper incompatible enhancement of the drill rotation constraint the sensitivity of displacement and stress results on the penalty parameter $\gamma = \beta\,\mu$, which was present in earlier contributions, can be eliminated. This is valid for a wide range of β, i.e., roughly, $1 \leq \beta \leq 10^6$.

Additionally, it has been shown that micropolar shell element formulations involving additional material parameters, which have to be determined by ad-hoc assumptions, do not yield better results in terms of accuracy and convergence rate. Moreover, it is demonstrated that the stiffness related to the nonsymmetric membrane strain plays the role of a penalty parameter rather than that of a material parameter. None of the numerical examples indicate the necessity of assuming nonsymmetric bending strains.

The new element formulation allows the application of nodal drill moments. In this context, the first-order shear correction factor β_w might deserve further investigation. There are indications that it is related to a non-local characteristic of the material behaviour.

REFERENCES

[1] H. Altenbach and V. A. V. A. Eremeyev. Actual Developments in the Nonlinear Shell Theory - State of the Art and New Applications of the Six-Parameter Shell Theory. In *Shell Structures: Theory and Applications, Vol. 3*. CRC Press/Balkema, 2014.

[2] U. Andelfinger and E. Ramm. EAS-elements for two-dimensional, three-dimensional, plate and shell structures and their equivalence to HR-elements. *Int. J. Numer. Methods Eng.*, 36(8):1311–1337, 1993.

[3] K. J. Bathe and E. N. Dvorkin. A formulation of general shell elements - the use of mixed interpolation of tensorial components. *Int. J. Numer. Methods Eng.*, 22(July 1985):697–722, 1986.

[4] Ted Belytschko, L. B. Wong, and H. Stolarski. Assumed Strain Stabilization Procedure For The 9 Node Lagrange Shell Element. *Int. J. Numer. Methods Eng.*, 28:385–414, 1989.

[5] P. G. Bergan and C.A. Felippa. A triangular membrane element with rotational degrees of freedom. *Comput. Methods Appl. Mech. Eng.*, 50:25–69, 1985.

[6] Erasmo Carrera, Salvatore Brischetto, and Pietro Nali. *Plates and Shells for Smart Structures: Classical and Advanced Theories for Modeling and Analysis*. 2011.

[7] Ismail Celik and Ozgur Karatekin. Numerical Experiments on Application of Richardson Extrapolation With Nonuniform Grids. *J. Fluids Eng.*, 119(3):584, 1997.

[8] Ismail Celik, Jun Li, Gusheng Hu, and Christian Shaffer. Limitations of Richardson Extrapolation and Some Possible Remedies. *J. Fluids Eng.*, 127(5):795–805, 2005.

[9] J. Chróścielewski, J. Makowski, and H Stumpf. Genuinely resultant shell finite elements accounting for geometric and material non-linearity. *Int. J. Numer. Methods Eng.*, 35(October 1991):63–94, 1992.

[10] J. Chróścielewski and Wojciech Witkowski. Four-node semi-EAS element in six-field nonlinear theory of shells. *Int. J. Numer. Methods Eng.*, 68(11):1137–1179, 2006.

[11] Robert D. Cook. Improved two-dimensional finite element. *J. Struct. Div.*, 100(9):1851–1863, 1974.

[12] E. N. Dvorkin and K. J. Bathe. A continuum mechanics based four-node shell element for general non-linear analysis, 1984.

[13] V. A. Eremeyev and W. Pietraszkiewicz. Phase transitions in thermoelastic and thermoviscoelastic shells. *Arch. Mech.*, 61(1):41–67, 2009.

[14] D.D. Fox and J. C. Simo. A drill rotation formulation for geometrically exact shells, 1992.

[15] A E Green and W Zerna. *Theoretical Elasticity*. Phoenix Edition Series. Dover Publications, 1969.

[16] F. Gruttmann and W. Wagner. A linear quadrilateral shell element with fast stiffness computation. *Comput. Methods Appl. Mech. Eng.*, 194:4279–4300, 2005.

[17] A Ibrahimbegovic. Stress resultant geometrically nonlinear shell theory with drilling rotations-Part I. A consistent formulation. *Comput. Methods Appl. Mech. Eng.*, 7825(94):265–284, 1994.

[18] S Klinkel, F. Gruttmann, and W. Wagner. A mixed shell formulation accounting for thickness strains and finite strain 3d material models. *Int. J. Numer. Methods Eng.*, 74(October 2007):945–970, 2008.

[19] N. F. Knight. Raasch challenge for shell elements. *AIAA J.*, 35(2):375–381, 1997.

[20] W T Koiter. A Consistent First approximation in the General Theory of Thin Elastic Shells. In D. G. Ashwell and W. T. Koiter, editors, *IUTAM Symp. Theory Thin Elastic Shells, Delft*, pages 12–33, North Holland, Amsterdam, 1959. Laboratorium voor Toegepaste Mechanica der Technische Hogeschool.

[21] A Libai and J. G. Simmonds. *The Nonlinear Theory of Elastic Shells*. Cambridge University Press, 2nd edition, 1998.

[22] G M Lindberg, M D Olson, and G R Cowper. New Developments in the Finite Element Analysis of Shells. Technical report, Structures and Materials Laboratory National Aeronautical Establishement, Ottawa, 1969.

[23] R. H. MacNeal and R. L. Harder. A proposed standard set of problems to test finite element accuracy. *Finite Elem. Anal. Des.*, 1:3–20, 1985.

[24] R. H. MacNeal, Charles T. Wilson, R. L. Harder, and Claus C. Hoff. The treatment of shell normals in finite element analysis. *Finite Elem. Anal. Des.*, 30:235–242, 1998.

[25] G. Rebel. *Finite Rotation Shell Theory Including Drill Rotations and Its Finite Element Implementations*. Phd dissertation, Delft University of Technology, 1998.

[26] Eric Reissner. Linear and nonlinear theory of shells. *Thin-shell Struct. Theory, Exp. Des.*, pages 29–44, 1974.

[27] Carlo Sansour and Herbert Bednarczyk. The Cosserat surface as a shell model, theory and finite-element formulation. *Comput. Methods Appl. Mech. Eng.*, 120(1-2):1–32, 1995.

[28] J. G. Simmonds. The Nonlinear Thermodynamical Theory of Shells: Descent from 3-Dimensions without Thickness Expansions. In E. L. Axerlrad and F. A. Emmerling, editors, *Flex. Shells, Theory Appl.* Springer-Verlag, 1984.

[29] J. G. Simmonds and Donald A Danielson. Nonlinear shell theory with finite rotation and stress-function vectors. *J. Appl. Mech.*, 39(4):1085–1090, 1972.

[30] J. C. Simo and F Armero. Geometrically non-linear enhanced strain mixed methods and the method of incompatible modes. *Int. J. Numer. Methods Eng.*, 33(2):1413–1449, 1992.

[31] J. C. Simo, F Armero, and R. L. Taylor. Improved versions of assumed enhanced strain tri-linear elements for 3D finite deformation problems. *Comput. Methods Appl. Mech. Eng.*, 110(2):359–386, 1993.

[32] J. C. Simo and D.D. Fox. On a stress resultant geometrically exact shell model. Part I: Formulation and optimal parametrization, 1989.

[33] J. C. Simo, D.D. Fox, and M.S. Rifai. On a stress resultant geometrically exact shell model. Part II: The linear theory; Computational aspects. *Comput. Methods Appl. Mech. Eng.*, 73:53–92, 1989.

[34] J. C. Simo, D.D. Fox, and M.S. Rifai. On a stress resultant geometrically exact shell model. Part III: Computational aspects of the nonlinear theory, 1990.

[35] J. C. Simo and M.S. Rifai. A class of mixed assumed strain methods and the method of incompatible modes. *Int. J. Numer. Methods Eng.*, 29(October 1989):1595–1638, 1990.

[36] W. Wagner and F. Gruttmann. A robust non-linear mixed hybrid quadrilateral shell element. *Int. J. Numer. Methods Eng.*, 64(October 2004):635–666, 2005.

[37] Krzysztof Wiśniewski. *Finite Rotation Shells Basic Equations and Finite Elements for Reissner Kinematics*. Springer, 2010.

[38] Krzysztof Wiśniewski and E Turska. Kinematics of finite rotation shells with in-plane twist parameter. *Comput. Methods Appl. Mech. Eng.*, 190:1117–1135, 2000.

[39] Krzysztof Wiśniewski and Ewa Turska. Recent Improvements in Hu-Washizu Shell Elements with Drilling Rotation. In *Shell-like Struct.*, pages 391–412. Springer, 2011.